Volume 55
Number 9
3 March 2026
Pages 3589-4002

Dalton Transactions

An international journal of inorganic chemistry

rsc.li/dalton

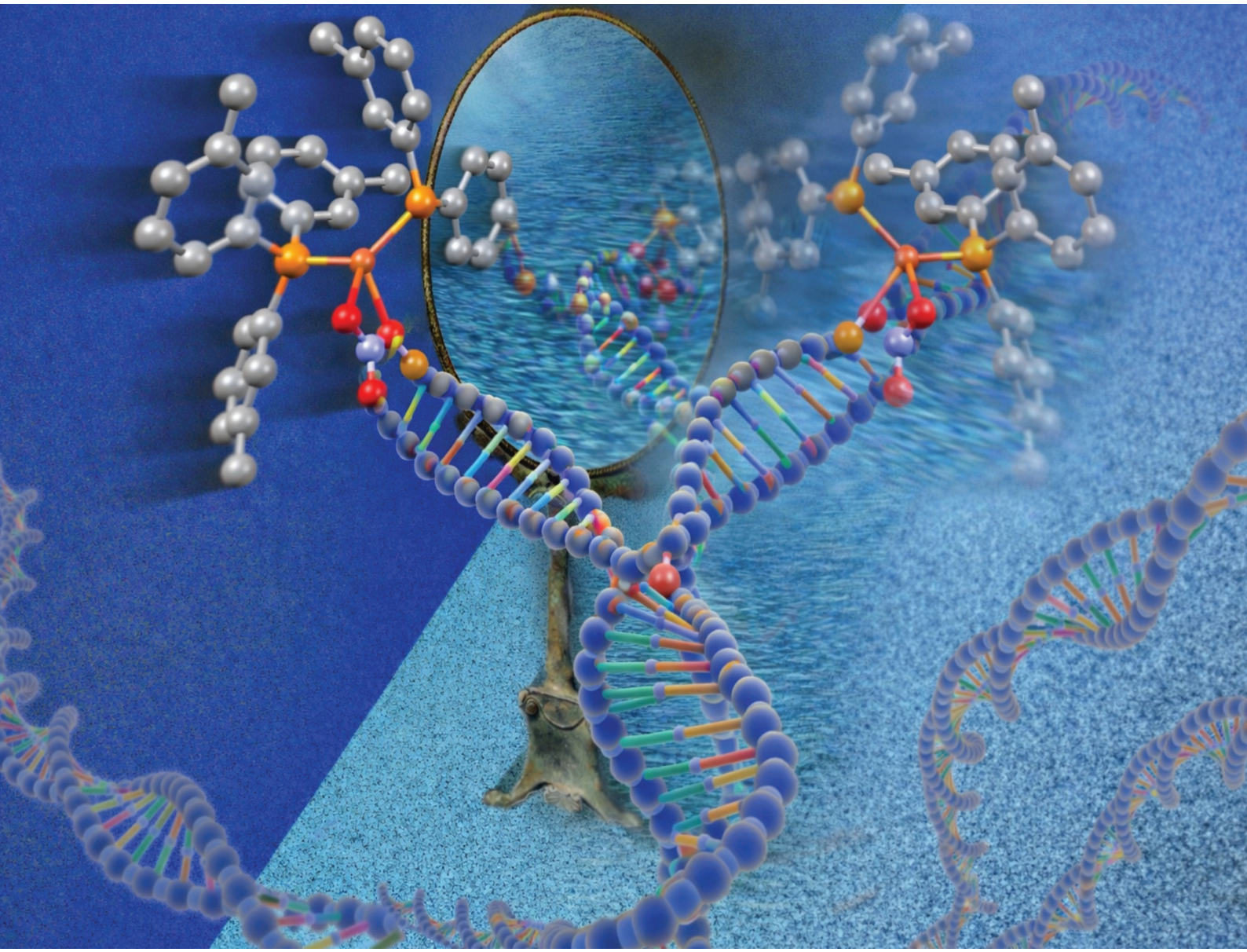

ISSN 1477-9226

ROYAL SOCIETY OF CHEMISTRY

PAPER

Sotiris Hadjikakou *et al.*

Chirality-controlled biomolecular recognition in Cu(I) metallodrugs: the first enantiomorphic CuP_2O_2 systems with dual DNA/LOX activity

Dalton Transactions

PAPER

View Article Online
View Journal | View Issue

Cite this: *Dalton Trans.*, 2026, **55**, 3687

Chirality-controlled biomolecular recognition in Cu(I) metallodrugs: the first enantiomorphic CuP_2O_2 systems with dual DNA/LOX activity

S. K. Hadjikakou, *[a] T. M. Koufou,[a] C. N. Banti, *[a] N. Tsoureas,[b] C. P. Raptopoulou,[c] V. Psycharis[c] and C. A. Mitsopoulou[b]

Received 4th December 2025,
Accepted 9th January 2026

DOI: 10.1039/d5dt02906f

rsc.li/dalton

Copper(II) nitrate reacts with tris(*m*-tolyl)phosphine (*m*-MePh)$_3$P in 1 : 2 and 1 : 3 molar ratios to form [Cu((*m*-MePh)$_3$P)$_2$(NO$_3$)] (**1**) which contains two isomers (**1A** and **1B**) in the crystal lattice and [Cu((*m*-MePh)$_3$P)$_3$(NO$_3$)] (**2**). The reaction of copper(II) nitrate with tris(*p*-tolyl)phosphine (*p*-MePh)$_3$P in 1 : 3 molar ratio results in the {[Cu((*p*-MePh)$_3$P)$_3$(NO$_3$)]·(DMF)·(H$_2$O)} (**3**) complex. The complexes were characterized in the solid state using melting point (m.p), X-ray fluorescence spectroscopy (XRF), and attenuated total reflectance-Fourier transform infra-red (ATR-FT-IR) spectroscopy, and in solution using cryoscopy, ultraviolet–visible (UV-vis) and nuclear magnetic resonance (^{1}H-NMR) spectroscopy. Their crystal structures were determined using single crystal X-ray crystallography in the solid state while the molecular weight was calculated using cryoscopy. A CCDC search shows that **1A** and **1B** are the first known chiral Cu(I) complexes of the CuP_2O_2 core. Binding affinity of complexes **1–3** toward calf thymus DNA (CT-DNA) was investigated *ex vivo* using UV-vis and fluorescence spectroscopy, viscosity measurements, and DNA denaturation assays. Their lipoxygenase (LOX) inhibitory activity was also studied. *In silico* computations further rationalized the DNA and LOX interactions with **1–3**. *In vitro* assays were conducted to evaluate the activity of **1–3** against human breast adenocarcinoma (MCF-7) cells, and the results are presented herein.

Introduction

Copper(I/II) is an essential trace element mainly distributed in mitochondrial enzymes such as cytochrome c and chaperones, playing a key role in cellular function.[1] Copper complexes are studied for numerous biological applications involving DNA interactions, including their use as DNA structural probes,[2] artificial nucleases[2–4] and DNA condensing agents for gene delivery.[5] Recently, copper complexes have been used as anticancer agents.[6,7] For example, casiopeina III-ia, [(aqua) (4,4′-dimethyl-2,2′-bipyridine) (acetylacetonato)copper(II)] nitrate, a unique copper-based antitumor drug, has entered phase I clinical trials in Mexico.[8] Moreover, copper(I) complexes have also been reported to act as enzyme inhibitors, particularly of topoisomerases I and II, as well as multi-protein proteasomes, leading to the death of cancer cells.[9] Because of their ability to cleave DNA efficiently, copper complexes represent promising anticancer agents and potential alternatives to platinum-based drugs.[10]

Because the interaction of anticancer agents with DNA is fundamental – governing their ability to disrupt essential processes such as replication and transcription – clarifying the principles that control this interaction is crucial for the rational design of new drugs. For this reason, complexes are designed with variations in steric volume, molecular weight, geometry, and electrostatic potential, aiming to fine-tune their binding affinity and selectivity toward DNA. These structural modifications allow the systematic study of steric and electronic effects that impose the mode and strength of DNA binding.[11–18]

Although copper chemistry is dominated by Cu(II) compounds due to the instability of Cu(I), the latter are highly relevant biologically.[8,19] Heteroleptic copper(I) complexes incorporating both phosphine and N,N-diimine ligands exhibit notable stability under aerobic conditions and display significant cytotoxic activity against tumor cells.[8] Stability is promoted by the strong interaction of soft P-donor atoms with the electron-rich Cu(I)-d^{10} metal center.[8]

In the course of our studies in the field of drug design and development of new chemotherapeutics which interact with DNA,[11–18,20–22] we report here the synthesis of the complexes with formulae [Cu((*m*-MePh)$_3$P)$_2$(NO$_3$)] (**1**) (two isomers co-crystallized, **1A** and **1B**), [Cu((*m*-MePh)$_3$P)$_3$(NO$_3$)] (**2**) and {[Cu((*p*-MePh)$_3$P)$_3$(NO$_3$)]·(DMF)·(H$_2$O)} (**3**), (*m*-MePh)$_3$P = tris(*m*-tolyl) phosphine and (*p*-MePh)$_3$P = tris(*p*-tolyl)phosphine (Scheme 1).

[a]*Biological Inorganic Chemistry Laboratory, Department of Chemistry, University of Ioannina, 45110 Ioannina, Greece. E-mail: shadjika@uoi.gr, cbanti@uoi.gr; Tel: +30-26510-08374, +30-26510-08362*
[b]*Inorganic Chemistry Laboratory, Department of Chemistry National and Kapodistrian University of Athens, Athens, Greece*
[c]*Institute of Nanoscience and Nanotechnology, NCSR "Demokritos", Athens, Greece*

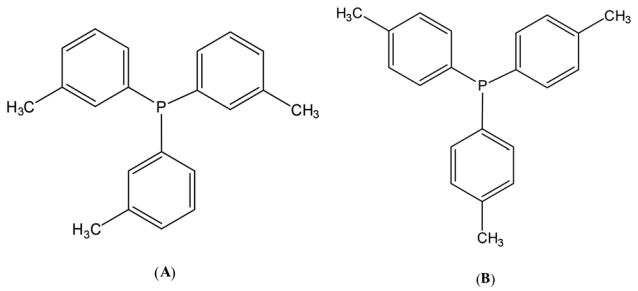

Scheme 1 Molecular diagrams of the ligands used (*m*-MePh)$_3$P (A) and (*p*-MePh)$_3$P (B).

The new agents were characterized using m.p., XRF, ATR-IR, cryoscopy, UV-vis and ^{1}H-NMR spectroscopy. The binding affinity of complexes **1–3** towards calf thymus DNA (CT-DNA) was investigated *ex vivo* using UV-vis, fluorescence spectroscopy, viscosity measurements, DNA denaturation assays and molecular docking computations. *Ex vivo* and *in silico* studies were also performed towards LOX. Moreover an *in vitro* assay was conducted to evaluate the activity of **1–3** against MCF-7 cells.

Results and discussion

General aspects

Aiming for the rationalization of the principles that govern the interaction of copper-based anticancer agents with DNA, three copper(I) complexes **1–3** were synthesized. The design of these compounds was based on the variation in the number of phosphine ligands coordinated to the copper center, as well as on the different steric volumes that each phosphine contributes to the complex. The Tolman cone angle, which provides a quantitative measure of the steric bulk (three-dimensional size) of a phosphine ligand around a metal center, is 136° for tris(*m*-tolyl) phosphine, (*m*-MePh)$_3$P, and 145° for tris(*p*-tolyl)phosphine, (*p*-MePh)$_3$P.[20,21] In addition, the electronic effect was modulated by the pK_a values of phosphines and the different coordination modes of the nitrate group, which acts as a monodentate ligand in the complexes containing three phosphines and as a chelating ligand in the complex bearing two phosphines. These compounds serve as precursor species for the subsequent preparation of a wide variety of copper(I) complexes.

Compounds **1 and 2** were obtained based on the different copper/phosphorus molar ratios in a MeOH/MeCN solvent system at 50 °C (Scheme 2, eqn (1) and (2)). Crystals of **1** were obtained from DMF, while those of **2** were obtained from DMSO. Compound **3** was obtained from DMF at 100 °C in 40 minutes (Scheme 2 (eqn (3))). The crystals were stored at room temperature. Complexes **1 and 2** are highly soluble in DMF and DMSO and soluble in CH_2Cl_2, $CHCl_3$, acetone, MeOH and MeCN while complex **3** is highly soluble in DMF and DMSO.

XRF spectroscopy

The XRF spectra of **1–3** confirm the presence of Cu in the complex (Fig. 1). The content of Cu in **1** was found to be 8.57 (±0.09)% w/w (calc. for ($C_{42}H_{42}CuNO_3P_2$): 8.66% w/w). The content of Cu in **2** was found to be 6.25(±0.09)% w/w (calc. for ($C_{63}H_{63}CuNO_3P_3$): 6.31% w/w). The corresponding content of Cu in the case of **3** was found to be 5.2(±0.27)% w/w (calc. for ($C_{66}H_{72}CuN_2O_5P_3$): 5.63% w/w).

Cryoscopy molecular weight (MW) measurements

The MWs of **1–3** were measured using cryoscopy in DMSO/ddw (1 : 49 v/v) solution with a freezing point osmometer. 1 μL solution of **1–3** (1 mg per 100 μL of DMSO) was diluted with 50 μL of double distilled water (ddw). The MWs were calculated to be 730.65 g mol^{-1} for **1** (calc. for [Cu((*m*-MePh)$_3$P)$_2$(NO$_3$)]: 733.44 g mol^{-1}), 1010.50 g mol^{-1} for **2** (calc. for [Cu((*m*-MePh)$_3$P)$_3$(NO$_3$)]: 1037.54 g mol^{-1}) and 1140.89 g mol^{-1} for **3** (calc. for {[Cu((*p*-MePh)$_3$P)$_3$(NO$_3$)]·(DMF)·(H$_2$O)}: 1129.75 g

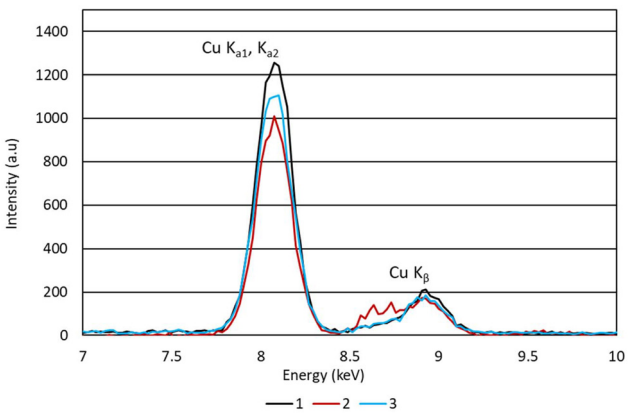

Fig. 1 XRF spectra of **1–3**. The Cu K_{a1}, K_{a2} peaks were used for quantitative determination of copper in the samples.

$$2\{[Cu(NO_3)_2]\,3H_2O\} + 5(m\text{-MePh})_3P \xrightarrow[50^\circ C]{MeOH/MeCN} 2[Cu((m\text{-MePh})_3P)_2(NO_3)] + (m\text{-MePh})_3P{=}O + 2\,HNO_3 + 2\,H_2O \quad \textbf{(Eq. 1)}$$

$$2\{[Cu(NO_3)_2]\,3H_2O\} + 7(m\text{-MePh})_3P \xrightarrow[50^\circ C]{MeOH/MeCN} 2[Cu((m\text{-MePh})_3P)_3(NO_3)] + (m\text{-MePh})_3P{=}O + 2\,HNO_3 + 2\,H_2O \quad \textbf{(Eq. 2)}$$

$$2\{[Cu(NO_3)_2]\,3H_2O\} + 7(p\text{-MePh})_3P \xrightarrow[100\text{-}150\ ^\circ C]{DMF} 2[Cu((p\text{-MePh})_3P)_3(NO_3)] + (p\text{-MePh})_3P{=}O + 2\,HNO_3 + 2\,H_2O \quad \textbf{(Eq. 3)}$$

Scheme 2 Synthetic route of **1–3**.

mol^{-1}). These values confirm the retention of the formulae in solution.

Solid state studies

Crystal and molecular structures of 1–3. The crystal structures of complexes **1–3** were determined using X-ray diffraction at 293(2) K. In the case of **1**, two isomers (**1A**) and (**1B**) were co-crystallized. Fig. 2 depicts the molecular structures of **1–3**, while selected bond distances and angles are summarized in the figure captions.

Single-crystal X-ray diffraction analyses revealed that the copper(I) complexes $[Cu((m\text{-}MePh)_3P)_2(NO_3)]$ (**1**), $[Cu((m\text{-}MePh)_3P)_3(NO_3)]$ (**2**), and $\{[Cu((p\text{-}MePh)_3P)_3(NO_3)]\cdot(DMF)\cdot(H_2O)\}$ (**3**) are all mononuclear species containing discrete molecules in the solid state. The coordination geometry around copper in all three complexes is distorted tetrahedral, with variations dictated by the number and steric profile of the coordinated phosphine ligands.

$[Cu((m\text{-}MePh)_3P)_2(NO_3)]$ (**1A** and **1B**) crystallizes in the orthorhombic, non-centrosymmetric and enantiomorphic space group $Pca2_1$ (no. 29) (Table 1). The absence of inversion and mirror symmetry in $Pca2_1$ implies that the crystal adopts a single handedness. Crystallization in $Pca2_1$ demonstrates that the coordination environment around Cu(I) (with two tris(*m*-tolyl)phosphines and nitrate) is chiral in the solid state; only one enantiomorphic form is present in the measured crystal, and the small, positive Flack value of 0.056(13), with low standard uncertainty, confirms the stereochemical sense reported. To the best of our knowledge and following a thorough search of the Cambridge Crystallographic Database, the structures of **1** (**1A** and **1B**) constitute the first reported examples of Cu(I) complexes that exhibit molecular chirality while simultaneously incorporating two phosphine ligands and a chelating nitrate group.[23] These structures therefore represent unique chiral Cu(I) species within this coordination motif. Two crystallographically independent isomeric complexes (**1A** and **1B**) occupy general positions and share the same absolute configuration, consistent with crystallization in an enantiomorphic space group.

The copper(I) center in the case of **1** is bound to two $(m\text{-}MePh)_3P$ ligands and one bidentate nitrate anion through two oxygen atoms, forming a CuP_2O_2 coordination sphere. The geometry approaches a slightly flattened tetrahedron with Cu–P bond lengths of approximately 2.21–2.22 Å and a longer Cu–O (NO_3) bond of about 2.24 Å. The steric congestion arising from the *m*-methyl substituents is accommodated by widening the P–Cu–P angle to *ca.* 129°, ensuring minimal intraligand repulsion.

Three tris(*m*-tolyl)phosphine ligands $(m\text{-}MePh)_3P$ coordinate to the Cu(I) center in **2**. The nitrate anion is bound in a monodentate manner through one oxygen atom. Consequently, the metal center adopts a pseudo-tetrahedral CuP_3O coordination environment. The Cu–P bond lengths are in the range of 2.29–2.32 Å, in agreement with those typically observed in Cu(I)-tris(aryl)phosphine complexes. The nitrate group interacts more loosely with copper than in **1**, indicating that the three bulky $(m\text{-}MePh)_3P$ ligands dominate the metal coordination environment and impose steric control over the geometry. The P–Cu–P angles in **2** (120.30(2)° (P1–Cu1–P2), 114.88(2)° (P3–Cu1–P1) and 111.76(2)° (P3–Cu1–P2)) are slightly wider/narrower (depending on actual values) than those of **1** (P2–Cu1–P1 = 129.29(5)°), reflecting the increased steric demand imposed by the three tris(*m*-tolyl)phosphine ligands around the Cu(I) center. This angular opening/compression is consistent with the more congested CuP_3O environment in **2** and highlights the steric modulation exerted by the phosphine framework compared with the CuP_2O_2 tetrahedral core observed in **1**.

Substitution of $(m\text{-}MePh)_3P_3$ with $((p\text{-}MePh)_3P)_3$ in **3** results in a slightly more symmetric tetrahedral geometry CuP_3O, due to the more extended and less sterically hindered *para*-methyl substituents. The Cu–P bonds (2.29–2.33 Å) are marginally longer than those in **1** and **2**, reflecting reduced steric strain and slightly stronger metal–phosphorus bonding. The nitrate again binds weakly through one oxygen atom, without bridging between copper centers. The coordination environment around the copper(I) centre in complex **3** displays the expected pseudo-tetrahedral geometry, defined by three phosphine donors and one oxygen atom of the nitrate ligand. The P–Cu–P angles in **3** are slightly compressed relative to those of **2**, reflecting the increased steric encumbrance imposed by the particular arrangement of the tris(aryl)phosphine ligands. This angular compression results in a more compact CuP_3O tetrahedral core. Similarly, the P–Cu–O angles in **3** are marginally narrower compared to those observed in **2**, consistent with the monodentate coordination of the nitrate oxygen and the steric crowding generated by the surrounding phosphine framework. Overall, the angular pattern in **3** indicates a slightly more distorted tetrahedral geometry than in **2**, driven predominantly by the steric profile of the phosphine ligands rather than electronic factors.

A comparative analysis of the crystallographic data of complexes **1A** and **1B** with those of previously reported Cu(I)-bis(phosphine)-nitrate structures in CCDC highlights their distinct structural features and establishes their uniqueness within this coordination family (Table 1).[23] Complexes **1A** and **1B** crystallize in the chiral space group $Pca2_1$, in contrast to their analogues (NITPPC01, NITPPC02, NITPPC20, YUYMIQ, and ZACZUY) (Table 1), which adopt centrosymmetric space groups (Table 1).[23–28] This chirality is directly reflected in their shorter and more compact Cu–P bond distances (2.22–2.23 Å), which are consistently shorter than those observed in the remaining structures (2.23–2.27 Å). The Cu–O distances fall within the expected range for bidentate nitrate coordination but exhibit a slightly more asymmetric distribution in **1A**/**1B**, consistent with a chiral perturbation of the CuP_2O_2 environment.

The P–Cu–P angles of **1A** and **1B** (129.3°–129.8°) lie between the most expanded values of the NITPPC series (130.9°–131.1°)[24–26] and the more compressed angle observed in YUYMIQ (126.33°)[27] (Table 1). More importantly, the P–Cu–O angles display a pronounced angular spread (104.6°–121.3°), significantly larger than the nearly symmetric angle pairs

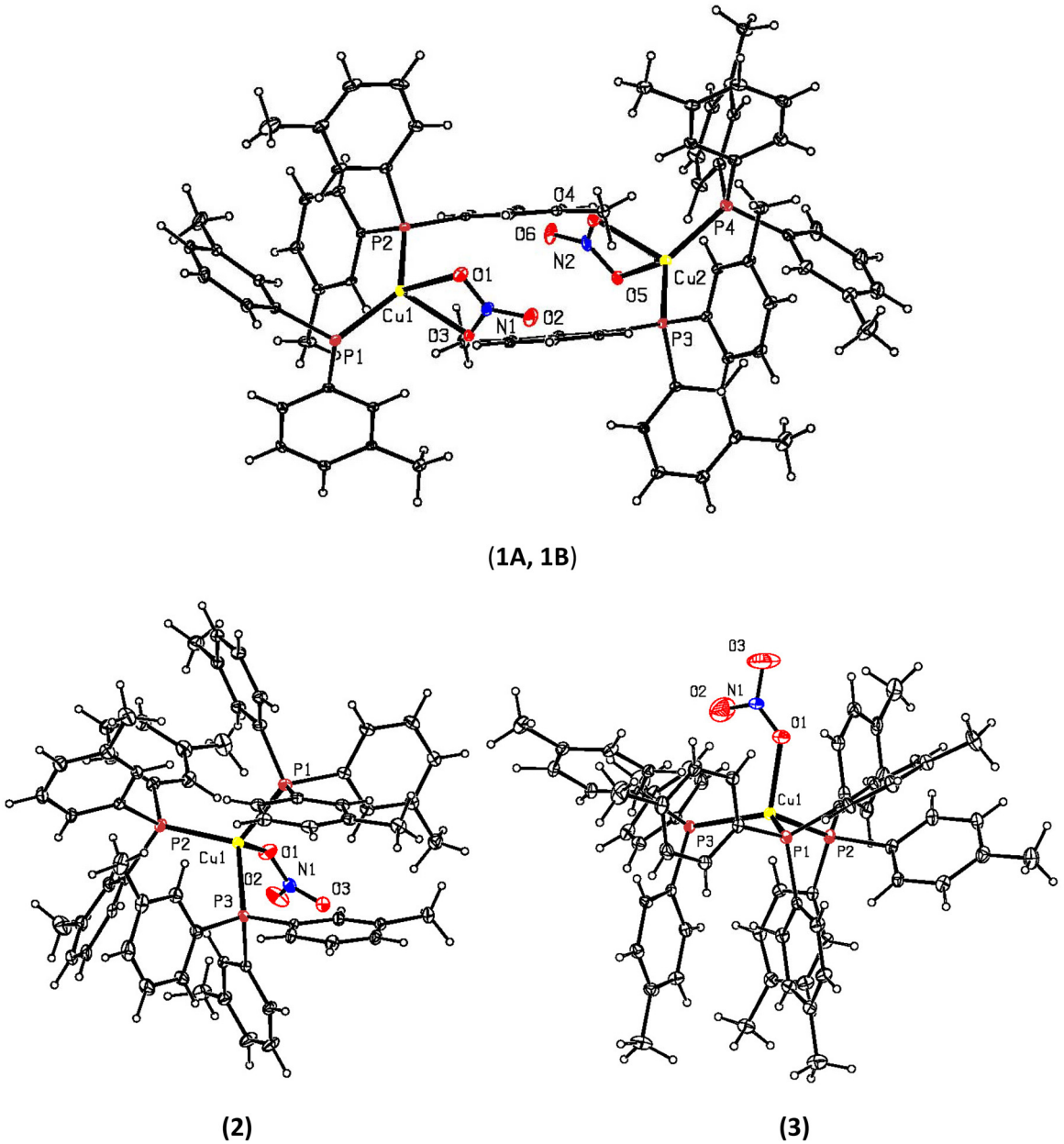

Fig. 2 Molecular structure of **1**. Selected bond lengths [Å] and angles [°]. Cu1–P1 = 2.2213(15), Cu1–P2 = 2.2200(14), Cu1–O1 = 2.234(4), Cu1–O3 = 2.177(3), Cu1–N1 = 2.578(4), Cu2–N2 = 2.572(4), Cu2–O5 = 2.174(3), Cu2–O4 = 2.221(4), Cu2–P3 = 2.2152(13), Cu2–P4 = 2.2257(16), O1–N1 = 1.262(6), O2–N1 = 1.230(6), O3–N1 = 1.264(6), O4–N2 = 1.268(6), O5–N2 = 1.266(5), O6–N2 = 1.229(6), P1–Cu1–P2 = 129.29(5), P1–Cu1–O1 = 121.28(12), P1–Cu1–O3 = 108.45(10), P1–Cu1–N1 = 119.78(12), P2–Cu1–O1 = 104.61(11), P2–Cu1–O3 = 113.49(10), P2–Cu1–N1 = 110.74(12), O1–Cu1–O3 = 58.58(13), O1–Cu1–N1 = 29.30(14), O3–Cu1–N1 = 29.32(13), P3–Cu2–N2 = 118.67(11), P4–Cu2–O4 = 104.57(11), P4–Cu2–O5 = 114.51(11), P4–Cu2–N2 = 111.43(11), O4–Cu2–O5 = 58.94(15), O4–Cu2–N2 = 29.54(15), O5–Cu2–N2 = 29.44(13), P3–Cu2–O4 = 117.22(11), P3–Cu2–O5 = 110.41(10), P3–Cu2–P4 = 129.82(5), O1–N1–O2 = 122.5(5), O1–N1–O3 = 117.4(4), O2–N1–O3 = 120.1(4), O5–N2–O6 = 121.1(5), O4–N2–O5 = 117.1(4), O4–N2–O6 = 121.8(4); molecular structure of **2**. Selected bond lengths [Å] and angles [°]. Cu1–P1 = 2.3217(7), Cu1–P2 = 2.3283(6), Cu1–P3 = 2.2963(6), Cu1–O1 = 2.1182(17), O1–N1 = 1.260(2), O2–N1 = 1.219(3), O3–N1 = 1.230(2), P1–Cu1–P2 = 120.30(2), P1–Cu1–P3 = 114.88(2), P1–Cu1–O1 = 103.94(5), P2–Cu1–P3 = 111.76(2), P2–Cu1–O1 = 98.29(5), P3–Cu1–O1 = 104.41(5), O1–N1–O2 = 118.1(2), O1–N1–O3 = 119.40(19), O2–N1–O3 = 122.4(2); molecular structure of **3**. Selected bond lengths [Å] and angles [°]. Cu1–P1 = 2.3287(12), Cu1–P2 = 2.3337(13), Cu1–P3 = 2.2960(13), Cu1–O1 = 2.120(5), O1–N1 = 1.159(7), O2–N1 = 1.277(10), O3–N1 = 1.170(9), P1–Cu1–P2 = 115.68(5), P1–Cu1–P3 = 114.45(5), P1–Cu1–O1 = 94.85(19), P2–Cu1–P3 = 114.37(5), P2–Cu1–O1 = 105.41(15), P3–Cu1–O1 = 109.63(14), O1–N1–O2 = 119.3(6), O1–N1–O3 = 132.3(7), O2–N1–O3 = 103.7(7).

found in the centrosymmetric NITPPC complexes,[24–26] where each P–Cu–O angle is mirrored by its inversion-related equivalent. This anisotropic angular distribution is a hallmark of the loss of inversion symmetry in **1A** and **1B** and directly reflects their intrinsic molecular chirality. Finally, the O–Cu–O angle is marginally wider in **1A**/**1B** (58.6–58.9°) relative to the

Table 1 Space groups along with bond lengths and angles of copper(I) nitrate phosphine deposited in CCDC[24–33]

	Space group	Cu1–P1	Cu1–P2	Cu1–P3	Cu1–O1	Cu1–O3	P1–Cu–P2	P1–Cu–P3	P2–Cu–P3	P1–Cu–O1	P1–Cu–O3	P2–Cu–O1	P2–Cu–O3	P3–Cu–O1	O1–Cu–O3
CuP_2O_2															
1A	$Pca2_1$	2.2213(15)	2.2200(14)		2.234(4)	2.177(3)	129.29(5)			121.28(12)	108.45(10)	104.61(11)	113.49(10)		58.58(13)
1B	$Pca2_1$	2.2152(13)	2.2257(16)		2.174(3)	2.221(4)	129.82(5)			117.22(11)	110.41(10)	104.57(11)	114.51(11)		58.94(15)
NITPPC01[24]	$C2/c$	2.2490(17)	2.2490(17)	—	2.197(5)	2.197(5)	130.87(6)	—	—	108.48(14)	114.29(14)	114.29(14)	108.48(14)	—	57.70(17)
NITPPC02[25]	$C2/c$	2.231(5)	2.231(5)	—	2.205(5)	2.205(5)	130.95(7)	—	—	114.45(9)	108.34(9)	108.34(9)	114.45(9)	—	57.35(10)
NITPPC20[26]	$I2/a$	2.256(2)	2.256(2)	—	2.222(2)	2.222(2)	131.11(7)			108.30(7)	114.30(7)	114.30(7)	108.30(7)		57.53(7)
YUYMIQ[27]	$P2_1/c$	2.2693(10)	2.2663(10)		2.193(3)		126.33(3)			106.45(10)		115.27(10)			
ZACZUY[28]	$P2_1/c$	2.253(4)	2.253(4)		2.215(12)	2.185(9)	128.03(12)			117.2(3)	116.3(2)	104.9(3)	111.9(2)		56.1(4)
CuP_3O															
2	$P2_1/c$	2.3217(7)	2.3283(6)	2.2963(6)	2.1182(17)		120.30(2)	114.88(2)	111.76(2)	103.94(5)	—	98.29(5)	—	104.41(5)	—
3	$P2_1/c$	2.3287(12)	2.3337(13)	2.2960(13)	2.120(5)		115.68(5)	114.45(5)	114.37(5)	94.85(19)	—	105.41(15)	—	109.63(14)	—
AHACER[29]	$P2_1/c$	2.2684(10)	2.2697(10)	2.3286(11)		2.070(3)	121.04(4)	112.79(4)	89.84(3)	109.87(8)	109.87(8)	116.26(8)			
BENGAE[30]	$P\bar{1}$	2.2901(5)	2.2840(5)	2.3257(5)	2.1182(13)		119.54(2)	115.77(2)	112.29(2)	112.11(4)		103.96(4)		87.93(4)	
BENGAE01[31]	$P\bar{1}$	2.2921(4)	2.2855(4)	2.3272(6)	2.1202(6)	—	119.51(2)	115.87(2)	112.34(2)	112.09(2)		103.96(2)		87.77(2)	
EFUWIM[32]	$P2_1/c$	2.3398(7)	2.3071(6)	2.3322(6)	2.1504(19)		121.70(2)	113.24(2)	113.80(2)	98.21(5)	—	109.78(6)	—	95.11(6)	—
FAKLIM[33]	$P2_1/c$	2.312(2)	2.337(2)	2.339(2)	2.174(5)	—	114.14(7)	121.37(7)	113.42(7)	109.53(13)	—	95.45(13)	—	97.93(13)	—

literature values (56.1–57.7°), indicating a slightly more open nitrate coordination, again attributable to the steric and geometric constraints imposed by the chiral phosphine arrangement. These observations demonstrate that **1A** and **1B** exhibit a uniquely distorted CuP_2O_2 tetrahedral core, distinct from all known Cu(I) bis(phosphine)nitrate complexes. Their shorter Cu–P distances, expanded and asymmetric P–Cu–O angles, and chiral space group clearly support their classification as the first structurally characterized chiral Cu(I) complexes bearing two phosphine ligands and a bidentate nitrate group.

The Cu(I) centre in complexes **2** and **3** adopts the expected pseudo-tetrahedral CuP_3O coordination environment, and their metrical parameters fall within the range reported in CCDC for related $CuP_3O(NO_3)$ species (AHACER, BENGAE, BENGAE01, EFUWIM, and FAKLIM)[29–33] (Table 1). The Cu–P bond lengths in **2** (2.2963–2.3283 Å) and **3** (2.2960–2.3337 Å) are slightly longer than those observed for AHACER[29] and the BENGAE/BENGAE01 [30,31] pair, but remain shorter or comparable to the most elongated Cu–P distances found in EFUWIM[32] and FAKLIM.[33] The Cu–O distances in **2** (2.1182 (17) Å) and **3** (2.120(5) Å) closely match those of the BENGAE[30] structures and lie between the shortest value observed for AHACER (2.070(3) Å)[29] and the more weakly bound nitrate ligands in EFUWIM[32] and FAKLIM (up to 2.174(5) Å),[33] indicating an intermediate Cu–O bond strength within the series.

The P–Cu–P angular pattern also reflects subtle but significant differences. In complex **2**, the P–Cu–P angles [120.30(2), 114.88(2) and 111.76(2)°] show a moderate angular spread, like those observed in the BENGAE/BENGAE01 systems,[30,31] whereas in **3** the three P–Cu–P angles [115.68(5), 114.45(5) and 114.37(5)°] are more homogeneous and cluster tightly around 115°, indicating a slightly more regular tetrahedral arrangement of the three phosphine donors. In contrast, AHACER[29] displays a strongly compressed P–Cu–P angle of 89.84(3)°, while EFUWIM[32] and FAKLIM[33] exhibit more pronounced angular opening (P–Cu–P up to *ca.* 114–121°), pointing to a higher degree of distortion in those structures. The P–Cu–O angles in **2** (98.29–104.41°) are centred close to 100°, whereas in **3** they span a wider range [94.85(19)–109.63(14)°], placing complex **3** in an intermediate position between the relatively symmetric P–Cu–O sets of EFUWIM/FAKLIM[32,33] and the more anisotropic distributions observed in AHACER[29] and BENGAE.[30,31] Overall, complexes **2** and **3** exhibit CuP_3O cores that are less distorted than those of AHACER and some of the more crowded analogues, with **3** in particular showing one of the most regular P_3 coordination environments within the examined Cu(I)-tris(phosphine)nitrate family.

Vibrational spectroscopy (ATR-FTIR)

The ν(H–$C_{aromatic}$) bands in the IR spectra of (*m*-MePh)$_3$P (3074(w) cm^{-1}) and (*p*-MePh)$_3$P (3069(w) cm^{-1})[34–37] are shifted at 3075(w) cm^{-1} in **1**, at 3074(w) cm^{-1} in **2** and at 3075 cm^{-1} in **3**, respectively (Fig. S1–S5). The ν(H–$C_{aliphatic}$) bands in the IR spectra of (*m*-MePh)$_3$P (2948, 2914(w) cm^{-1}) and (*p*-MePh)$_3$P (2944, 2920(w) cm^{-1}) are observed, respectively,[34–37] and remain unshifted in the case of **1–3**.

The $\nu_{as}(NO_3^-)$ and $\nu_s(NO_3^-)$ vibrational bands are observed at 1431 (vs) and 1017 (vs) cm^{-1} in the case of copper(II) nitrate salt.[38] The $\nu_s(NO_3^-)$ is shifted at 1020 (m) cm^{-1} in **1**, at 1019 (m) cm^{-1} in **2** and at 1018 (m) cm^{-1} in **3**.

The ν_{as}(C–P) and ν_s(C–P) in the spectrum of free (*m*-MePh)$_3$P are found at 777, 693 (vs) cm^{-1} and at 446, 438 (vs) cm^{-1}. The corresponding ν_{as}(C–P) and ν_s(C–P) in the spectrum of free (*p*-MePh)$_3$P are observed at 707, 660 (m) cm^{-1} and at 513, 501 (vs) cm^{-1}. These bands are observed at 780, 693 (s) cm^{-1} and at 455, 451 (m) cm^{-1} in the case of **1**, at 779, 693 (s) cm^{-1} and at 455, 436 (s) cm^{-1} in the case of **2**. The ν_{as}(C–P) and ν_s(C–P) in the case of **3** are found at 711, 658 (m) cm^{-1} and at 511, 496 (vs) cm^{-1}.

Solution studies

[i] *Stability of the complexes in solution*: The stability of complexes **1–3** in DMSO solution was confirmed by UV-vis and ^{1}H-NMR spectroscopy (Fig. S6–S11). No changes were observed in their spectra after 48 h. [ii] *UV-vis spectroscopy*: the spectra of **1–3** in DMSO solutions are dominated by absorption bands at 268 (**1**), 268 (**2**) and 266 (**3**) nm, with molar extension coefficients (ε) of 15 280 (**1**), 14 072 (**2**) and 22 900 (**3**) cm^{-1} M^{-1}, respectively, (Fig. S6–S8). The spectra of (*m*-MePh)$_3$P and (*p*-MePh)$_3$P in DMSO show absorption bands at 268 (ε = 11 183 cm^{-1} M^{-1}) and 266 nm (ε = 9991 cm^{-1} M^{-1}). [iii] *^{1}H-NMR spectroscopy*: Table 2 summarizes the resonance signals observed in the ^{1}H-NMR spectra of complexes **1–3** in comparison with their free ligands. The aromatic protons (H[$C_{aromatic}$]) of (*m*-MePh)$_3$P exhibit an upfield shift upon coordination to the Cu(I) ion in complexes **1** and **2**, whereas for the (H[$C_{aromatic}$]) of (*p*-MePh)$_3$P, a downfield shift is observed in **3**. The *o*- and *m*-aromatic protons in complex **3** obviously "collapse". This is because in *para*-substituted aryl rings, the aromatic protons form an AA′BB′ system (*o* and *m* sets). In the spectrum of **3**, the chemical-shift separation between these two sets is small, and the resonances are further affected by second-order behavior and ^{31}P–^{1}H long-range coupling, leading to significant overlap. As a result, the *o*- and *m*-signals appear as a single merged multiplet at the resolution shown. The methyl protons of the tolylphosphines (H[*m*-CH_3] or H[*p*-CH_3]) display an upfield shift in complexes **1** and **2**, while they remain unshifted in **3**.

Biological studies

Chirality has a significant influence on the design and synthesis of medicines, as the database shows that about 50% of drugs launched so far contain stereochemical elements.[39] The presence of chirality in receptors and enzymes demands stereoselective interaction of drug molecules. Employment of single enantiomers in medical treatment has brought asymmetric synthesis as a major theme in drug discovery. Because chirality is fundamental in biological systems – where most biomolecules are asymmetric and function depends on precise three-dimensional geometry – we examined the DNA-binding properties and LOX inhibitory activity of complex **1** and compared them with complexes **2** and **3**. These findings were then correlated with their respective effects on cell proliferation.

Table 2 ^{1}H-NMR resonance signals in the spectra of **1–3** and their ligands

Compound	H[$C_{aromatic}$] (ppm)	H[*m* or *p*-CH_3] (ppm)
(*m*-MePh)$_3$P	7.49–6.96	2.26
1A/1B	7.27–7.01	2.13
2	7.29–7.01	2.13
(*p*-MePh)$_3$P	7.22–7.08	2.31
3	7.19–7.13	2.32

In vitro cell studies

The cytotoxic evaluation of compounds **1–3** against the MCF-7 breast cancer cell line revealed IC_{50} values in the range of 3.6–4.1 μM, demonstrating considerably higher antiproliferative potency compared to cisplatin (IC_{50} = 5.5 μM) (Table 3). In particular, compound **1** exhibits the strongest activity (IC_{50} = 3.6 μM), outperforming not only cisplatin but also many previously reported copper-based metallodrugs (Table 3). Earlier classes of Cu(I) complexes typically display IC_{50} values between 6 and 20 μM against MCF-7 cells, depending on the geometry, lipophilicity, and DNA-binding characteristics of the complex (Table 3). When compared to these literature-reported systems, compounds **1–3** fall within the highly active category, showing 2–5-fold stronger activity than classical Cu(I) coordination compounds.[18,40] Compounds **2** and **3**, while slightly less active, still maintain IC_{50} values superior to that of cisplatin and comparable to or better than those of the most active mononuclear or dinuclear copper complexes previously described in the literature (Table 3). These findings highlight the promising anticancer potential of this new family of copper compounds.

Calf thymus (CT-DNA) binding affinity

The binding affinity of complexes **1–3** towards CT-DNA was investigated using [i] UV-vis and [ii] fluorescence spectroscopy, as well as [iii] viscosity and [iv] DNA denaturation studies. The results were further rationalized by molecular docking calculations performed with the AutoDock software package.

UV absorption spectroscopic studies. There are three main types of non-covalent interactions of complexes with CT-DNA: (a) groove binding (minor or major grooves), (b) intercalative binding mode and (c) electrostatic interactions.[14–20,40–42] Changes in the DNA double helix conformation lead to hypochromic or hyperchromic effects. Hypochromism is typically associated with intercalative or electrostatic modes of interaction, whereas hyperchromism is indicative of groove binding or hydrogen bond cleavage.[14–20,40–42]

In the case of the titration of CT-DNA with **1–3**, the percentage of hyperchromism at λ_{max} = 258 nm recorded is 9.8% for **1**, 8.7% for **2** and 9.5% for **3** with no shift in λ_{max} (Fig. 3).

These results suggest that complexes **1–3** interact with CT-DNA primarily through a groove-binding mode rather than by hydrogen bond cleavage, since the hyperchromic effect is below 40%.[14–20,40–42] The binding constant (K_b) of **1–3** with CT-DNA was determined by titrating the complex solutions

Table 3 Antiproliferative activity against MCF-7 cells (IC_{50}, μM) determined using *in vitro* cytotoxicity assays (SRB assay); binding affinity toward CT-DNA (K_b values, M^{-1}) evaluated using UV-vis absorption titration; inhibitory activity against lipoxygenase (LOX) (IC_{50}, μM) determined using UV spectroscopy; and binding energies toward DNA and LOX (kcal mol^{-1}) obtained from *in silico* molecular docking studies for complexes **1–3**

	MCF-7 IC_{50} (μM)	K_b ($\times 10^4$) M^{-1}	Binding energy (DNA) (kcal mol^{-1})	LOX IC_{50} (μM)	Binding energy (LOX) (kcal mol^{-1})	Ref.
1A/1B	3.6 ± 0.2	12.6 ± 0.9	−8.04/−6.26	13.1	−5.26/−4.68	[a]
2	4.1 ± 0.2	8.8 ± 0.8	−3.35	26.4	−2.12	[a]
3	4.1 ± 0.1	9.2 ± 0.2	−2.92	28.9	−2.20	[a]
[Cu(SalH)(tpp)$_3$] 1a	2.4 ± 0.1	5.1 ± 0.8	−2.84	8.7 ± 0.2	−1.50	40
[Cu(SalH)(tpp)$_3$] 1b	4.0 ± 0.3	10.5 ± 1.7	−2.01	5.7 ± 0.6	−0.68	40
[Cu(tpSb)$_3$Cl]	11.1 ± 0.4	14.4 ± 1.1	−3.85	—	—	18
[Cu$_2$(tpSb)$_4$Br$_2$]	9.2 ± 0.5	14.2 ± 1.7	−3.57	—	—	18
[Cu$_2$(tpSb)$_4$I$_2$]	18.4 ± 1.4	12.0 ± 3.9	−2.69	—	—	18
Cisplatin	5.5 ± 0.4	—		65.9		18

[a] In this study, $SalH_2$ = salicylic acid, tpp = triphenylphosphine, and tpSb = triphenylantimony.

with CT-DNA and monitoring the changes in absorbance in the UV-vis spectra (300–310 nm) as the CT-DNA concentration increased (Fig. 3). K_b values were obtained from the slope and intercept of the Wolfe–Shimer equation, based on the linear correlation of $[DNA]/(\varepsilon_a - \varepsilon_f)$ *vs.* $[DNA]$[14–20,40–42] (Fig. 3). The K_b values are $(12.0 \pm 0.9) \times 10^4$ M^{-1} (**1**), $(8.8 \pm 0.8) \times 10^4$ M^{-1} (**2**) and $(9.2 \pm 0.2) \times 10^4$ M^{-1} (**3**) suggesting mild interaction between the DNA binders and CT-DNA (Table 3).

Fluorescence spectroscopic studies. The binding properties of **1–3** towards DNA were also studied using fluorescence spectroscopy. Ethidium bromide (EB) is a strong intercalator to DNA and it emits intense fluorescent light upon its conjugation with DNA. The CT-DNA–EB complex emits at λ_{max} = 588 nm upon its excitation at λ_{ex} = 527 nm (ref. 14–20 and 40–42) and the fluorescence spectra of the CT-DNA–EB compound with increasing concentrations of agents are shown in Fig. 4.

The binding (K_{app}) constants were calculated using eqn (4):[14–20,40–42]

$$K_{EB}[EB] = K_{app}[drug], \quad (4)$$

where [drug] is the concentration of the agent at a 50% reduction of the fluorescence $K_{EB} = 10^7$ M^{-1}, and the concentration of [EB] is 2.3 μM.

The linear plot of I_0/I_x *vs.* the concentration of **1–3** leads to the equation from where the concentration of the drug at a 50% reduction of the fluorescence is derived (Fig. 4). I_0 and I_x are the intensities of radiation emitted from the CT-DNA–EB complex in the absence and presence of **1–3**. The calculated K_{app} values are $(4.7 \pm 0.4) \times 10^4$ M^{-1}, $(4.9 \pm 0.3) \times 10^4$ M^{-1} and $(6.2 \pm 0.2) \times 10^4$ M^{-1} for **1–3**, respectively. The K_{app} values are in the range between 10^4 and 10^5 M^{-1}, suggesting a groove binding mode of **1–3** towards CT-DNA.[14–20,40–42] In contrast, the K_{app} value higher than 10^6 M^{-1} suggests an intercalation mode (*e.g.* ethidium bromide binds to DNA with an affinity of 10^7 M^{-1}).[14–20,40–42] This binding mode is also confirmed using the corresponding results from UV-vis spectroscopic studies.

Viscosity studies. The viscosity of a DNA solution is highly sensitive to structural changes of the DNA itself. Therefore, viscosity of a DNA solution is widely employed to investigate the binding modes of agents interacting with it. Upon binding of a molecule to DNA, the length of the DNA is altered, which in turn affects the viscosity of the solution.[40–42] Specifically: [i] intercalation results in a significant increase in the relative viscosity of the DNA–agent solution, due to unwinding and elongation of the DNA double helix;[40–42] [ii] groove binding or electrostatic interactions, in contrast, do not markedly change the DNA length, leading to minimal effects on viscosity;[40–42] [iii] cleavage of the DNA strands by an agent produces shorter DNA fragments, resulting in a notable decrease in viscosity;[40–42] and [iv] covalent bond formation between an agent and DNA, as seen in cisplatin–DNA complexes, induces bending of the DNA backbone, shortening the helical axis and thus decreasing the solution's viscosity.[40–42]

Fig. 5 shows the comparison of the relative specific viscosity values, $(\eta/\eta_0)^{1/3}$, for the ratio r = [complex]/[DNA]. The DNA's solution viscosity remains unchanged to a significant extent upon increasing the concentration of **1–3**, either by decreasing or increasing it, suggesting possible groove binding or electrostatic interactions with DNA.[40–42] In order to ascertain the groove binding of the compounds towards DNA, the viscosity of their solutions is compared with the corresponding one of the minor groove binders or intercalators (such as minor groove binding agent Hoechst 33258 and intercalator EB (Fig. 5)). For DNA lengthening studies, the plot of $(\eta/\eta_0)^{1/3}$ *versus* r yields a slope close to 1 (φ = 45°) for a "classical" intercalator (such as EB).[42,43] This can be explained by the fact that in B-form DNA, each base pair contributes approximately 3.4 Å to the helical axis. Upon intercalation, the agent inserts between two adjacent base pairs, forcing them apart and thereby extending the DNA helix by about 3.4 Å. Thus, each intercalation event corresponds to the addition of one more base-pair spacing. This elongation of the DNA double helix results in an increase of the solution's viscosity, which is a characteristic feature of the intercalative binding mode. Nevertheless, most classical intercalators (EB) typically yield slopes in the range of 0.5–1 (φ = 30°) in such plots (Fig. 5).[42,43] Classical groove binders, on the other hand, such as Hoechst 33258, typically result in a slope of 0 (φ = −4°). For complexes **1–3**, the linear correlation of $(\eta/\eta_0)^{1/3}$ *versus* r yielded φ values

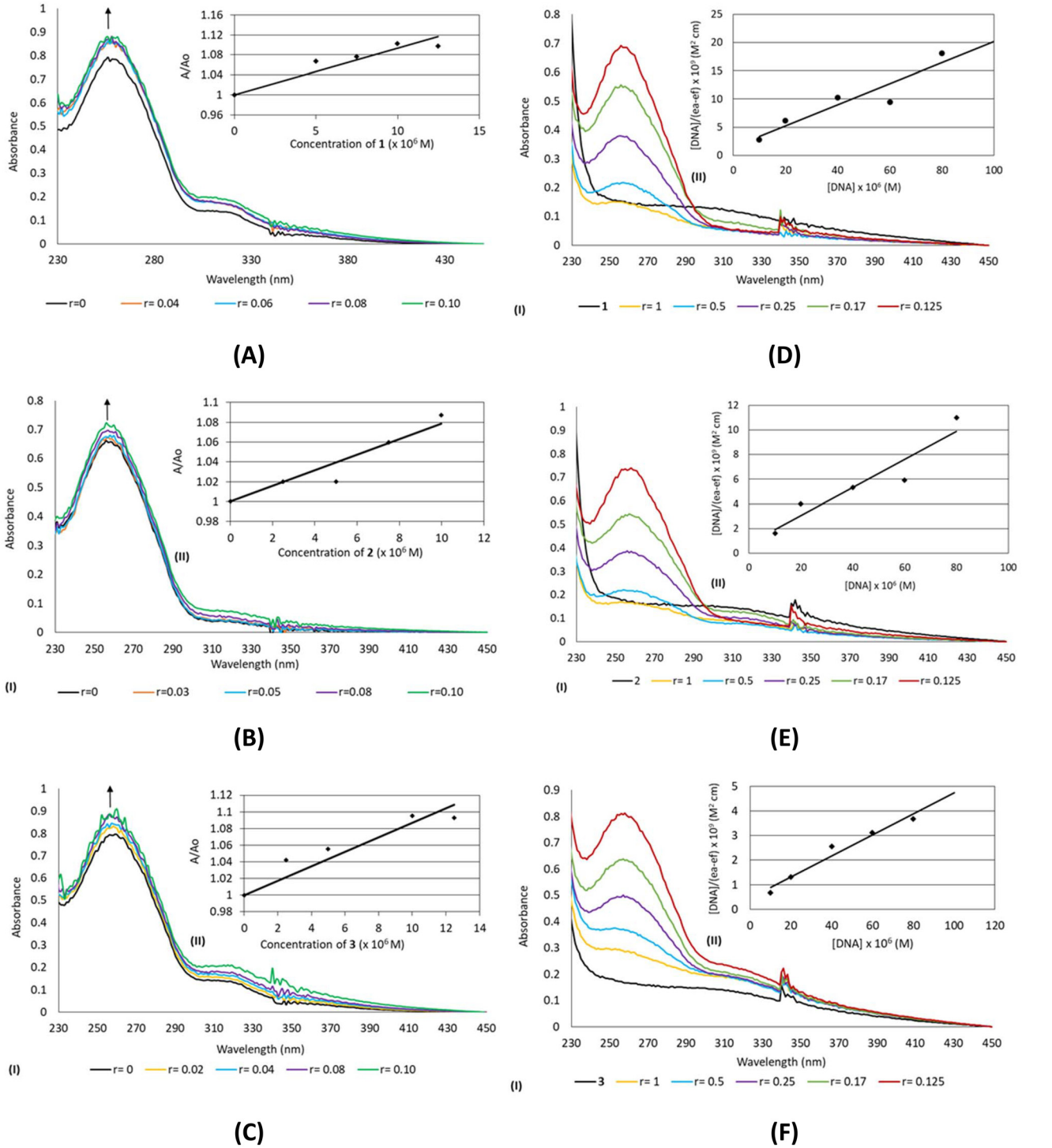

Fig. 3 (I) UV-vis titration spectra of CT-DNA buffer solution in the absence and presence of complexes **1** (A), **2** (B), and **3** (C) at various r values (0–0.10; r = [complex]/[DNA], [DNA] = 1 × 10^{-4} M). (II) Plot of A/A_0 *vs.* [complex] at 258 nm. UV-vis titration spectra of complexes **1** (D), **2** (E), and **3** (F) solutions in the absence and presence of CT-DNA at r values 1, 0.5, 0.25, 0.17, and 0.125 (r = [complex]/[DNA], [complex] = 50 μM, [CT-DNA] = 10–80 μM). Graphical plot of [DNA]/($\varepsilon_a - \varepsilon_f$) *vs.* [DNA].

of 12°, 15°, and −22°, which are in closer agreement with the φ values typically observed for groove-binding agents (0° for groove binders in contrast to 45° of intercalators). These results are consistent with the groove-binding mode of interaction with DNA, as concluded for compounds **1–3** from UV-vis and fluorescence spectroscopic studies (Fig. 5).

DNA thermal denaturation study. DNA thermal denaturation studies provide information about the binding mode and the

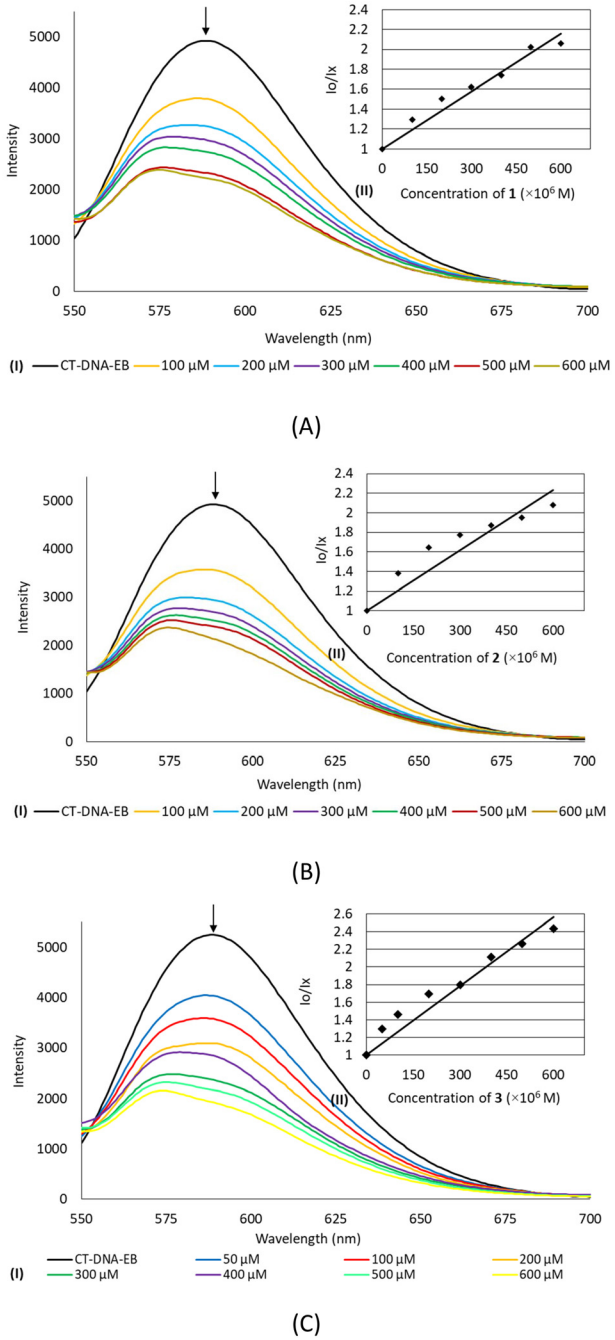

Fig. 4 (I) The emission spectrum of the CT-DNA–EB complex under excitation at λ_{ex} = 527 nm in the presence of **1(A)–3(C)** ([EB] = 2.3 μM, [DNA] = 26 μM, [**1–3**] = 0–600 μM). The arrow indicates the change in intensity with increasing complex concentration. The inset II displays plots of emission intensity I_o/I_x against [agent].

strength of the drug–DNA interaction. A hyperchromic effect is observed in the absorption spectra at λ_{max} = 258 nm with increasing temperature, indicating disruption of base-stacking interactions and hydrogen bonding between the bases of double-stranded DNA. As a consequence, a characteristic sigmoidal melting transition curve is obtained.

The DNA melting temperature (T_m) is defined as the temperature at which 50% of the double-stranded DNA dissociates into single strands.[40–42] The T_m value of CT-DNA is determined from the midpoint of the melting transition, which is obtained by plotting the relative absorbance (f_{ss}) as a function of temperature. The relative absorbance is defined as $f_{ss} = (A - A_{min})/(A_{max} - A_{min})$, where A represents the absorbance of the CT-DNA–drug solution at a given temperature T, A_{min} is the minimum absorbance, and A_{max} is the maximum absorbance.[40–42]

Fig. 6 shows the DNA thermal denaturation curves in the absence and in the presence of **1–3**. The T_m value for free CT-DNA is 59.5 ± 1.0 °C, while the T_m values in the presence of **1–3** are 55.0 ± 0.9 (**1**), 56.3 ± 0.4 (**2**) and 53.8 ± 0.4 (**3**) °C, respectively. The effect of **1–3** on the melting profile of CT-DNA (ΔT_m) value is lower than 2 °C, suggesting either a groove or electrostatic interaction mode of **1–3** towards CT-DNA. Intercalators on the other hand, such as EB, cause a considerable increase of the T_m of DNA leading to higher ΔT_m values (ΔT_m = 13 °C for EB).[40–42]

In silico studies – DNA docking

Inhibition of DNA replication and transcription through the binding of metal complexes, such as cisplatin, has significantly advanced the field of metallotherapeutics.[14,15] To explore the potential DNA-binding mode of **1A**, **1B**, **2** and **3**, DNA docking studies were performed against the self-complementary B-DNA dodecamer d(CpGpCpGpApApTpTpCpGpCpG) (PDB ID: 1BNA)[44] using AutoDockTools software package. The results indicate that **1A**, **1B**, **2** and **3** preferentially dock into the minor groove (GC-rich sequence region), likely due to their non-rigid molecular structure (Fig. 7). The binding energies of **1A**, **1B**, **2** and **3** towards oligonucleotide are −8.04 (**1A**), −6.26 (**1B**), −3.35 (**2**) and −2.92 (**3**) kcal mol^{-1}, respectively. This ordering can be rationalized by the combined action of electronic polarization of the nitrate group and steric/shape complementarity mainly of tris(*m*-/*p*-tolyl)phosphine ligands. The GC-rich minor groove is narrower and exhibits a more negative electrostatic potential along its walls, which favors interaction with the polarized nitrate group and facilitates contacts from the aryl rings of the phosphine ligands surrounding the tetrahedral Cu(I) center. Complex **1A** fully exploits this complementarity, with **1B** to a somewhat lesser extent, while complex **2** interacts only moderately and complex **3** fails to approach adequately due to steric congestion.

In the case of **1A**, the O1 atom of the nitrate group interacts with the C1 carbon atom of the DC21 nucleobase, located deep within the minor groove [*d*(O1···C(DC21)) = 3.169 Å], while the phenyl rings of the phosphine ligands remain relatively flexible (Fig. 7). However, in the case of **1B**, the O6 atom of the nitrate group interacts with the N2 atom of the DG4 nucleobase, within the minor groove [*d*(O6···N(DG4)) = 2.919 Å] (Fig. 7). For complex **2**, the O3 atom of the nitrate group interacts with the C1 atom of the DC23 nucleobase [*d*(O3···C1(DC23)) = 2.867 Å]. No significant interaction was detected in the case of **3** (Fig. 7).

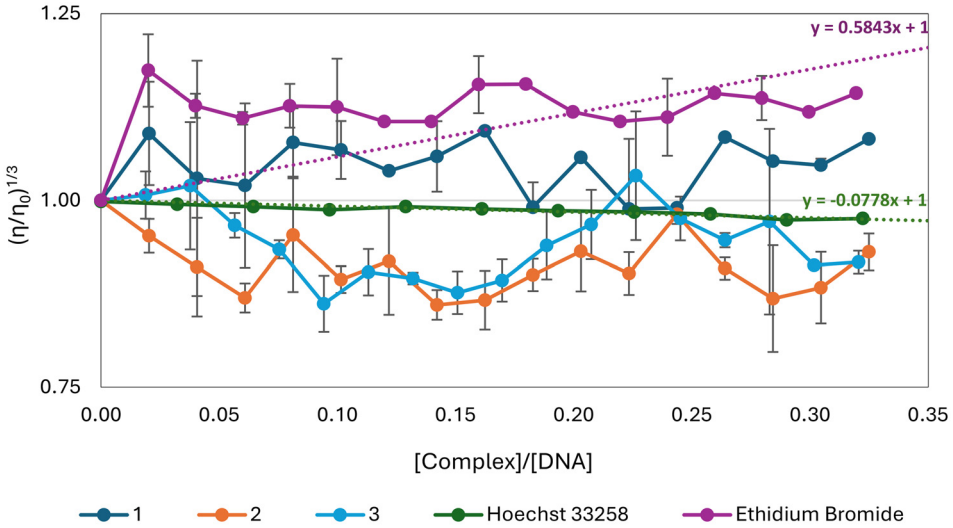

Fig. 5 Relative viscosity of CT-DNA solutions with increasing concentrations of **1–3**, Hoechst 33258 and ethidium bromide, respectively ([DNA] = 10 mM, r = [compound]/[DNA], η is the viscosity of DNA in the presence of the compounds and η_0 is the viscosity of DNA alone).

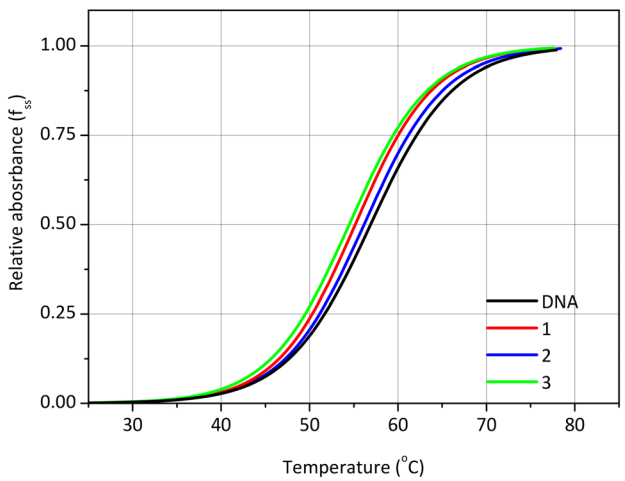

Fig. 6 Melting curves of CT-DNA in the absence and presence of **1–3**, CT-DNA = 2.0 × 10^{-5} M; C_{drug} = 10^{-6} M in 1 mM trisodium citrate, 10 mM NaCl (pH = 7.0). Diagram of relative absorbance (f_{ss}) *vs.* temperature (f_{ss} = $(A - A_{min})/(A_{max} - A_{min})$, where A_{min} is the minimal absorbance of the solution of CT-DNA–drug, at a temperature T, A is the absorbance of CT-DNA–drug corresponding to a specific temperature and A_{max} is the maximum absorbance of CT-DNA–drug, respectively).

Study of 1–3 inhibitory activity toward the peroxidation of linoleic acid by the LOX enzyme

Lipoxygenase (LOX) plays a critical role in the metabolism of arachidonic acid to leukotrienes, which are key lipid mediators involved in inflammation, immune responses, and cell-signaling pathways.[11–20,40–42] Through regio- and stereo-specific oxygenation of polyunsaturated fatty acids, LOX isoforms generate hydroperoxy derivatives that serve as precursors for leukotrienes, lipoxins, and other bioactive eicosanoids. These metabolites regulate diverse biological processes, including inflammatory cell recruitment, vascular permeability, and oxidative stress responses. LOX activity dysfunction has been associated with tumor progression, chronic inflammatory diseases, asthma and neurodegeneration, making LOX an important therapeutic target in drug discovery.[11–20,40–42,45] Particularly in breast cancer, elevated LOX activity promotes angiogenesis, invasion, and metastatic dissemination. In pancreatic cancer, LOX contributes to a pro-inflammatory tumor microenvironment and enhances survival signaling pathways. In prostate cancer, LOX is involved in activating pathways that drive proliferation, tumor progression, and resistance to therapy.[45]

Fig. 8 illustrates the relationship between LOX activity (A%) and the negative logarithm concentration ($p\log(C)$) of **1–3**.

As a result, the inhibitory activity of **1–3** was evaluated toward the peroxidation of linoleic acid by LOX enzyme. The compounds **1–3** show significant reduction in LOX catalytic activity, giving IC_{50} values of 13.1 (**1**), 26.4 (**2**) and 28.9 (**3**) μM, respectively. These values demonstrate higher inhibitory activity compared to cisplatin (IC_{50} = 65.9 μM), 5-fold for **1**, 2.5-fold for **2** and 2.3-fold for **3**.

In silico studies LOX docking

Molecular docking studies were also employed to rationalize the binding efficacy of **1–3** towards LOX. The binding energies of **1–3** along with their binding pockets towards LOX are determined (Table 3 and Fig. 9).

The docking data reveal a strong influence of chirality on the way Cu(I) complexes engage the LOX enzyme, both in terms of binding affinity and the nature of the amino-acid residues forming their binding pockets. The chiral complexes **1A** and **1B** bind significantly closer to the catalytic Fe center (Fe···Cu distances 27.8 Å and 25.3 Å, respectively) than the achiral complexes **2** and **3**, which bind much more distantly (39.9–40.5 Å). This closeness correlates with clearly more favor-

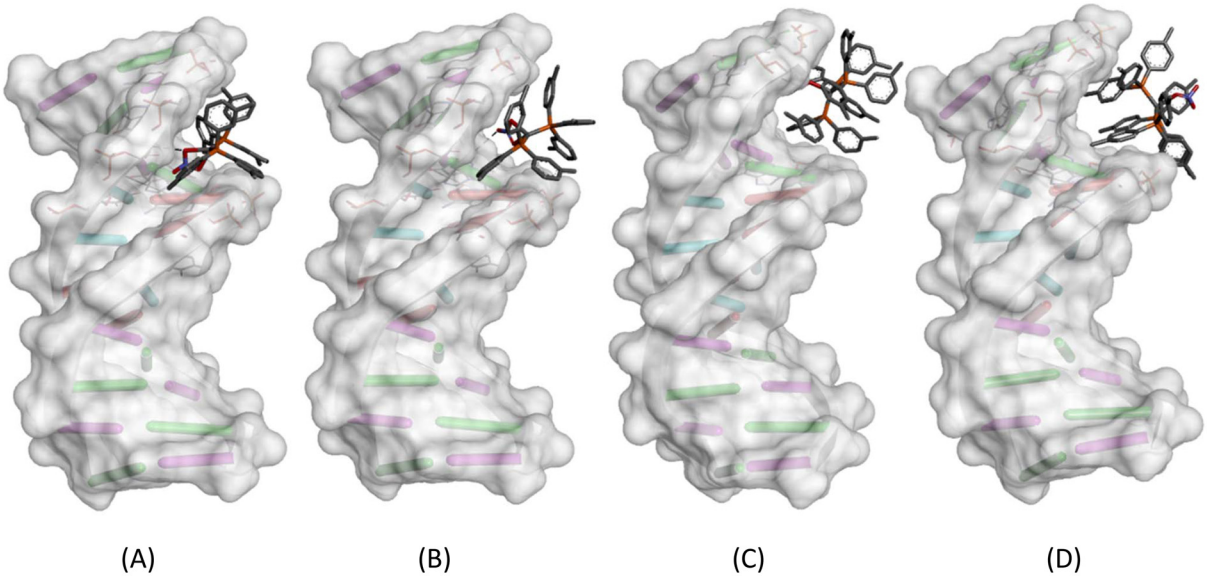

Fig. 7 Predicted minor groove binding sites of complexes **1A** (A), **1B** (B), **2** (C) and **3** (D) on DNA (*in silico* analysis).

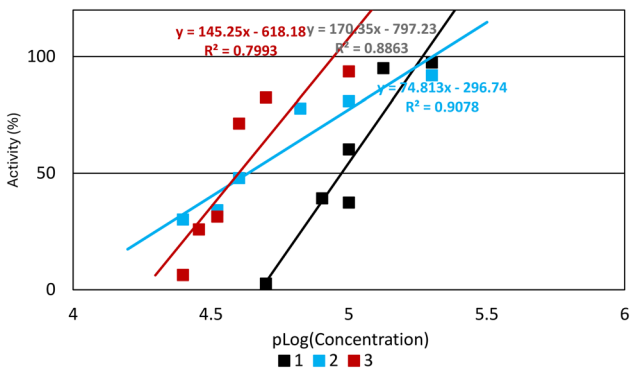

Fig. 8 LOX activity (*A*%) *vs.* negative logarithm of inhibitor (**1–3**) concentration (*p* log(*C*)).

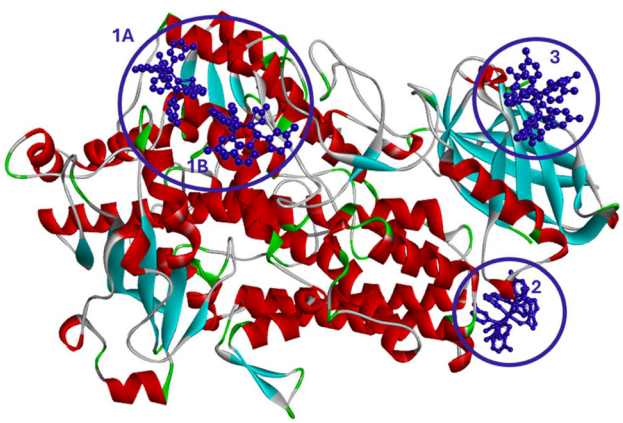

Fig. 9 Binding sites of the studied inhibitors **1–3**.

able binding energies for **1A** (−5.26 kcal mol^{-1}) and **1B** (−4.68 kcal mol^{-1}) compared to **2** and **3** (−2.12 and −2.20 kcal mol^{-1}), demonstrating that chirality enhances both complementarity and intermolecular stabilization within the LOX cavity. The binding energy of **1–3** towards LOX follows the order **1A** < **1B** < **3** < **2**, which indicates the LOX inhibitory activity trend **1A** > **1B** > **3** > **2**. The corresponding order of binding energy of **1–3** in DNA is determined as **1A** < **1B** < **2** < **3**, suggesting that the order of affinity of **1–3** towards DNA is **1A** > **1B** > **2** > **3**. Experimentally, the IC_{50} values of **1–3** against LOX follow the order **1A**/**1B** < **2** < **3** (inhibitory activity of **1–3** against LOX **1A**/**1B** > **2** > **3**), while the corresponding K_b values for CT-DNA binding follow the trend **1A**/**1B** > **3** > **2**. The IC_{50} values against MCF-7 cells further show the order **1A**/**1B** < **2** ≈ **3**. Taken together, the computational and experimental results reveal a coherent structure–activity relationship, with complexes **1A** and **1B** consistently exhibiting the highest biological performance across all evaluated targets. Both docking energies and experimental IC_{50} values demonstrate that **1A**/**1B** are the most potent LOX inhibitors and the strongest DNA binders, confirming the reliability and significance of these measurements.

The binding pockets of **1A** and **1B** are also broader, chemically richer, and more structurally complex than those sampled by **2** and **3**. Complex **1A** interacts with a highly cooperative binding environment composed of Asp228, Glu565, Val205, Phe212, Pro204, Lys561, and Tyr562, enabling simultaneous hydrogen-bonding, electrostatic, and hydrophobic contacts. Complex **1B**, although docked into a different region, also engages a dense network of residues, Glu271, Asp275, Leu742, Ala426, Phe274, and Pro743, forming a well-defined hydrophobic-polar pocket that stabilizes binding. These multisite interactions arise from the asymmetric three-dimensional orientation of the chiral CuP_2 core, which allows the phos-

phine aryl rings and the nitrate substituent to adopt conformations that fit more precisely into the grooves of the LOX surface.

In contrast, the achiral CuP_3O complexes **2** and **3** engage significantly simpler and more diffuse binding pockets, reflecting poorer geometric complementarity. Complex **2** interacts mainly with Lys777, Glu153, His147, Tyr149, and Tyr632, with no deep insertion into a defined cavity, while complex **3** interacts only with Lys138, indicating a largely superficial association with the enzyme surface. These limited interactions correspond to their lower binding affinities, demonstrating that the expanded, sterically crowded CuP_3O geometry reduces the ability of **2** and **3** to orient themselves effectively within LOX pockets.

Overall, the data clearly show that chirality and a compact CuP_2O_2 coordination framework enable **1A** and **1B** to access deeper, better-defined, and more chemically diverse binding pockets in LOX, leading to significantly stronger binding. In contrast, the achiral and more sterically overloaded CuP_3O complexes (**2**, **3**) are restricted to peripheral pockets, resulting in weaker stabilization and reduced biological activity. These findings highlight the role of stereochemistry and coordination compactness in directing selective molecular recognition within enzymatic environments.

Conclusion

This work demonstrates that variations in coordination geometry, Cu–P bond strength, and stereochemistry have a decisive impact on the biological profile of Cu(I) phosphine complexes. The chiral complexes **1A** and **1B**, characterized by the shortest Cu–P bond distances and crystallization in the non-centrosymmetric $Pca2_1$ space group, exhibit a compact CuP_2O_2 coordination environment that enhances both electronic interaction and their steric complementarity with biomolecular targets. These structural attributes correlate directly with their superior biological activity, reflected in the lowest IC_{50} values against MCF-7 cells, the strongest DNA-binding affinities, and the most favorable DNA and LOX docking energies within the entire series.

In contrast, the achiral CuP_3O complexes **2** and **3**, which possess longer Cu–P bond distances and crystallize in the centrosymmetric $P2_1/c$ space group, show significantly weaker interactions with DNA and LOX and display correspondingly reduced cytotoxic potency. The expanded, sterically overloaded CuP_3O environment appears less capable of adopting the precise three-dimensional orientation required for efficient minor-groove binding or for interacting productively with the LOX binding pocket.

The excellent agreement between experimental data (IC_{50}, K_b, viscosity, and ΔT_m) and computational predictions (DNA/LOX docking energies and binding geometries) further confirms that the biological performance of these complexes is governed by a synergy of structural compactness, electronic polarization, and stereochemical organization. The chiral complexes **1A** and **1B** emerge as potent dual-target agents, simultaneously binding DNA and inhibiting LOX more effectively than both their achiral analogues and cisplatin.

Overall, this study establishes a clear structure–activity relationship in which chirality, shorter Cu–P bonding, and a well-defined CuP_2O_2 geometry collectively enhance biomolecular recognition and biological efficacy. These findings provide a compelling foundation for the development of next-generation chiral Cu(I)-based anticancer agents and set the stage for future investigations into enantioselective interactions, mechanistic pathways, and *in vivo* therapeutic potential of this promising class of metallotherapeutics.

Experimental

Materials and instruments

All solvents used were of reagent grade, and tris(tolyl)phosphines and copper(II) nitrate (Aldrich, Merck) were used with no further purification. Elemental analyses for C and H were carried out with a Carlo Erba EA model 1108 instrument. Mid-infrared spectra (4000–400 cm^{-1}) were obtained on a Cary 670 FTIR spectrometer (Agilent Technologies). A UV-1600 PC series spectrophotometer of VWR was used for the recording of electronic absorption spectra. The fluorescence spectra were recorded on a Jasco FP-8200 fluorescence spectrometer. ^{1}H-NMR spectra were recorded on a Bruker AC 400 MHz FT-NMR instrument in DMSO-d_6 solution. Chemical shifts are reported in ppm using TMS as an internal reference. XRF measurement was also carried out with a Rigaku NEX QC EDXRF analyzer (Austin, TX, USA). Cell lines for cell screening experiments were purchased from the American Type Culture Collection (ATCC, Rockville, MD, USA).

Synthesis and crystallization of 1–3

Preparation of complexes **1** and **2**: a solution of 0.2 mmol of $Cu(NO_3)_2{\cdot}3H_2O$ (0.048 g) in 10 mL of acetonitrile was added to a 10 mL methanolic solution of 0.5 mmol of (m-MePh)$_3$P (0.152 g) in the case of **1** and 0.7 mmol of (m-MePh)$_3$P (0.212 g) for **2**. The bluish solutions were stirred at 50 °C until they gradually turned colorless. The clear solution was filtered off, and the filtrate was concentrated to dryness. The white powder obtained was washed with 5 mL of diethylether and it crystallized in DMF (**1**) and DMSO (**2**), respectively. Crystals of **1 and 2** suitable for X-ray analysis were grown from slow evaporation of the solutions. In the case of **3**, 0.2 mmol of $Cu(NO_3)_2{\cdot}3H_2O$ (0.048 g) and 0.7 mmol of (p-MePh)$_3$P (0.212 g) were directly stirred in 10 mL of DMF at 100 °C for 40 minutes and the clear solution was kept in darkness. Crystals of **3** suitable for X-ray analysis were grown from slow evaporation of the solution.

1: colorless crystal, melting point: 73–75 °C; elemental analysis found: C: 68.55; H: 5.55; N: 1.64, Cu: 8.57%; calculated for $C_{42}H_{42}CuNO_3P_2$: C: 68.71; H: 5.76; N: 1.91; Cu: 8.66%; IR (cm^{-1}): 3336 (br), 2918 (m), 1659 (s), 1591 (s), 1481 (m), 1444 (vs), 1400 (m), 1285 (vs), 1218 (m), 1172 (m), 1105 (s), 1027

(m), 995 (m), 891 (m), 780 (vs), 689 (vs), 545 (vs), 452 (vs); ^{1}H-NMR (ppm) in DMSO-d_6: 7.27–7.01 (m, $C_{aromatic}$), 2.13 (s, *m*-CH_3 group); UV-vis (DMSO): λ = 268 nm (log ε = 4.18).

2: colorless crystal, melting point: 150–151 °C; elemental analysis found: C: 75.28; H: 6.73; N: 1.30; Cu: 6.25%; calculated for $C_{63}H_{63}CuNO_3P_3$: C: 75.10; H: 6.30; N: 1.39; Cu = 6.31%; IR (cm^{-1}): 3384 (br), 1655 (m), 1591 (m), 1480 (m), 1443 (s), 1285 (vs), 1218 (m), 1172 (m), 1106 (s), 1022 (vs), 952 (s), 891 (m), 780 (vs), 694 (vs), 546 (vs), 452 (vs); ^{1}H-NMR (ppm) in DMSO-d_6: 7.29–7.01 (m, $C_{aromatic}$), 2.13 (s, *m*-CH_3 group); UV-vis (DMSO): λ = 268 nm (log ε = 4.15).

3: colorless crystal, melting point: 169–170 °C; elemental analysis found: C: 77.28; H: 6.88; N: 2.45; Cu: 5.2%; calculated for $C_{66}H_{72}CuN_2O_5P_3$: C: 77.17; H: 6.42; N: 2.48; Cu: 5.63%; IR (cm^{-1}): 3433 (br), 2921 (m), 2114 (m), 1656 (m), 1597 (s), 1496 (s), 1441 (s), 1395 (m), 1285 (vs), 1186 (s), 1097 (vs), 1021 (s), 803 (vs), 709 (s), 643 (m), 628 (s), 612 (m), 511 (vs), 493 (vs), 433 (s); ^{1}H-NMR (ppm) in DMSO-d_6: 7.19–7.13 (m, $C_{aromatic}$), 2.32 (s, *p*-CH_3 group); UV-vis (DMSO): λ = 266 nm (log ε = 4.36).

X-ray structure determination

Single crystals of **1–3** suitable for crystal structure analysis were obtained by slow evaporation of their mother liquids at room temperature. Data for **1 and 2** were collected using a Bruker D8-Venture dual source (Cu/Kα and Mo/Kα) SC-XRD instrument equipped with a 4-circle kappa goniometer and Photon-III area detector, using φ and ω scans to fill the Ewald sphere. In both cases, data were collected using Mo/Kα at 100 K to a resolution of 0.75 Å. Data collection strategy, acquisition, integration and scaling were performed using the APEX4 software suite and packages within. Structure solution,[46] modelling and refinement[47] were achieved *via* their implementation into the Olex2-1.5 [48] software suite. Non-H atoms were refined anisotropically, using weighted full-matrix least-squares on F^2 while H-atoms were added using the riding model with SHELXL default parameters unless otherwise stated.

Single-crystal X-ray diffraction data of **3** were collected using a Rigaku R-AXIS SPIDER Image Plate diffractometer utilizing graphite monochromated Mo Kα radiation. Cell refinement, data reduction and empirical absorption corrections were applied using the CrystalClear program package.[49] The crystal structure of **3** was solved by direct methods using SHELXS v.2013/1 and refined on F^2 using full-matrix least squares techniques with SHELXL ver.2014/6.[46,47] All non-hydrogen atoms were refined anisotropically whereas hydrogen atoms were admitted ideal positions and refined as riding on respective atoms.[50]

Crystallographic data (excluding structure factors) for the structures reported in this paper have been deposited with the Cambridge Crystallographic Data Centre as supplementary publication no. CCDC 2486986 (**1**), 2486987 (**2**) and 2490244 (**3**).

1: $C_{42}H_{42}CuNO_3P_2$, MW = 734.24, orthorhombic, space group *Pca*21, a = 20.5014(11), b = 10.9874(8), c = 33.168(2) Å, V = 7471.3(8) Å^3, Z = 8, ρ(calc) = 1.306 g cm^{-3}, μ = 0.710 mm^{-1}, F(000) = 3072. 405 166 reflections measured, 18 584 unique (R_{int} = 0.125). The final $R1$ = 0.0512 (for 16 927 reflections with $I > 2s(I)$) and w$R(F2)$ = 0.1223 (all data) S = 1.12.

2: $C_{63}H_{63}CuNO_3P_3$, MW = 1038.59, monoclinic, space group *P*21/*c*, a = 22.0146(7), b = 10.9051(4), c = 23.8047(7) Å, β = 112.006(1)°, V = 5298.5(3) Å^3, Z = 4, ρ(calc) = 1.302 g cm^{-3}, μ = 0.550 mm^{-1}, F(000) = 2184. 154 228 reflections measured, 13 168 unique (R_{int} = 0.072). The final $R1$ = 0.0409 (for 10 692 reflections with $I > 2s(I)$) and w$R(F2)$ = 0.1136 (all data) S = 1.04.

3: $C_{66}H_{72}CuN_2O_5P_3$, MW = 1070.12, monoclinic, space group *C*2, a = 22.5150(13), b = 11.0851(5), c = 23.7237(12) Å, β = 96.669 (2)°, V = 5880.9(5) Å^3, Z = 4, ρ(calc) = 1.209 g cm^{-3}, μ = 0.526 mm^{-1}, F(000) = 2120. 22 994 reflections measured, 11 053 unique (R_{int} = 0.076). The final $R1$ = 0.0757 (for 7699 reflections with $I > 2s(I)$) and w$R(F2)$ = 0.2192 (all data) S = 1.05.

Biological tests

DNA binding studies. CT-DNA was diluted in a buffer containing 15 mM trisodium citrate and 150 mM NaCl at pH 7 and stirred for several days at 4 °C.[14–20,40–42] The absorbance of the DNA stock solution yielded anA_{260}/A_{280} ratio between 1.8 and 1.9, indicating that the DNA was sufficiently free from protein contamination.[14–20,40–42] The concentration of CT-DNA was determined by measuring absorbance at 260 nm, using an extinction coefficient of 6600 M^{-1} cm^{-1}.[14–20,40–42] UV-vis spectroscopy measurements, fluorescence studies, viscosity measurements and DNA denaturation studies were performed as previously reported.[14–20,40–42]

Study of the peroxidation of linoleic acid by the enzyme lipoxygenase in the presence of 1–3. This study was carried out as previously reported.[11–20,40–42]

SRB assay. Stock solutions of **1–3** (0.01 M) were dissolved in DMSO and diluted with cell culture medium to the suitable concentrations (0.5–30 μM). MCF-7 cells were plated in 96-well flat-bottom microplates at various cell inoculation densities at 6000 cells per well. These cells were incubated for 24 h at 37 °C and they were exposed to **1–3** for 48 h. The evaluation of the cytotoxicity of the compounds was carried out by means of SRB colorimetric assay at λ = 568 nm by using the percent of the surviving cells against the control ones (untreated cells). The SRB assay was carried out as previously described.[14–22,40–42]

Docking studies. AutodockVina[51] was used for the molecular docking studies along with the graphical interface AutodockTools (ADT 1.5.7).[52] The DNA structure remained rigid while no torsional restraints were applied to the complexes. Prior to docking, water molecules and crystallized solvents were removed. The docking search space was enclosed in a grid box extended to cover the entire DNA structure allowing maximum flexibility for the ligands. The default values of the software were used for the calculations.[11–15] For LOX *in silico* studies, the PDB ID: 1F8N was used, according to previously procedure described in ref. 11–15. The output graphics were produced by Discovery Studio 2001.

Author contributions

Conceptualization: S. K. H.; supervision: S. K. H.; investigation: T. M. K., N. T., C. P. R., V. P., and C. A. M.; methodology:

C. N. B., C. P. R., V. P., C. A. M. and S. K. H.; validation: S. K. H.; writing – original draft: C. N. B. and S. K. H.; writing – review and editing: C. N. B. and S. K. H. All authors have read and agreed to the published version of the manuscript.

Conflicts of interest

There are no conflicts to declare.

Data availability

The data supporting the findings of this study are available within the article and its supplementary information (SI). Supplementary information is available. See DOI: https://doi.org/10.1039/d5dt02906f.

Additional raw data (spectroscopic files, crystallographic datasets, and computational output) are available from the corresponding author upon reasonable request.

CCDC 2486986, 2486987 and 2490244 contain the supplementary crystallographic data for this paper.[53a–c]

Acknowledgements

This work was carried out in fulfilment of the requirements for the master's thesis of Ms T. M. K. according to the fulfilment of the International Graduate Program in "Biological Inorganic Chemistry", which operates at the University of Ioannina within the collaboration of the Departments of Chemistry of the Universities of Ioannina, Athens, Thessaloniki, Patras, Crete and the Department of Chemistry of the University of Cyprus (https://bic.chem.uoi.gr/BIC-En/index-en.html) under the supervision of Prof. S. K. H.

References

1 L. K. Wood and D. J. Thiele, Transcriptional Activation in Yeast in Response to Copper Deficiency Involves Copper-Zinc Superoxide Dismutase, *J. Biol. Chem.*, 2009, **284**, 404–413.
2 A. Erxleben, Interactions of copper complexes with nucleic acids, *Coord. Chem. Rev.*, 2018, **360**, 92–121.
3 C. Wende, C. Lüdtke and N. Kulak, Copper complexes of N-donor ligands as artificial nucleases, *Eur. J. Inorg. Chem.*, 2014, 2597–2612.
4 A. G. Papavassiliou, Chemical nucleases as probes for studying DNA-protein interactions, *Biochem. J.*, 1995, **305**, 345–357.
5 G.-Y. Li, R.-L. Guan, L.-N. Ji and H. Chao, DNA condensation induced by metal complexes, *Coord. Chem. Rev.*, 2014, **281**, 100–113.
6 C. Santini, M. Pellei, V. Gandin, M. Porchia, F. Tisato and C. Marzano, Advances in copper complexes as anticancer agents, *Chem. Rev.*, 2014, **114**, 815–862.
7 A. Erxleben, Advances in the development of DNA-cleaving metal complexes as anticancer agents, in *Elsevier Reference Module in Chemistry, Molecular Sciences and Chemical Engineering*, ed. J. Reedijk, Elsevier, Waltham, MA, 2015, pp. 413–476, DOI: 10.1016/B978-0-12-409547-2.11594-X.
8 U. K. Komarnicka, S. Kozieł, P. Zabierowski, R. Kruszyński, M. K. Lesiow, F. Tisato, M. Porchia and A. Kyzioł, Copper(I) complexes with phosphines P(p-OCH_3-Ph)$_2CH_2OH$ and P(p-OCH_3-Ph)$_2CH_2$SarGly. Synthesis, multimodal DNA interactions, and prooxidative and *in vitro*, antiproliferative activity, *J. Inorg. Biochem.*, 2020, **203**, 110926.
9 R. A. Khan, M. Usman, R. Dhivya, P. Balaji, A. Alsalme, H. AlLohedan, F. Arjmand, K. AlFarhan, M. A. Akbarsha, F. Marchetti, C. Pettinari and S. Tabassum, Heteroleptic Copper(I) Complexes of "Scorpionate" Bis-pyrazolyl Carboxylate Ligand with Auxiliary Phosphine as Potential Anticancer Agents: An Insight into Cytotoxic Mode, *Sci. Rep.*, 2017, **7**, 45229.
10 L. Qian, T. Miao and L. Xu, Probing DNA-Cleavage Efficiencies of Copper(II) Complexes: A Computational Perspective, *ACS Omega*, 2020, **5**, 19029–19033.
11 M. N. Xanthopoulou, S. K. Hadjikakou, N. Hadjiliadis, E. R. Milaeva, J. A. Gracheva, V.-Y. Tyurin, N. Kourkoumelis, K. C. Christoforidis, A. K. Metsios, S. Karkabounas and K. Charalabopoulos, Biological Studies of New Organotin(IV) Complexes of Thioamide Ligands, *Eur. J. Med. Chem.*, 2008, **43**, 327–335.
12 S. Zartilas, S. K. Hadjikakou, N. Hadjiliadis, N. Kourkoumelis, L. Kyros, M. Kubicki, M. Baril, I. S. Butler, S. Karkabounas and J. Balzarini, Tetrameric 1:1 and monomeric 1:3 complexes of silver(I) halides with tri(p-tolyl)-phosphine: A structural and biological study, *Inorg. Chim. Acta*, 2009, **362**, 1003–1010.
13 G. K. Batsala, V. Dokorou, N. Kourkoumelis, M. J. Manos, A. J. Tasiopoulos, T. Mavromoustakos, M. Simčič, S. Golič-Grdadolnik and S. K. Hadjikakou, Copper(I)/(II) or silver(I) salts towards 2-mercaptopyrimidine; An exploration of a chemical variability with possible biological implications, *Inorg. Chim. Acta*, 2012, **382**, 146–157.
14 C. N. Banti, A. D. Giannoulis, N. Kourkoumelis, A. M. Owczarzak, M. Poyraz, M. Kubicki, K. Charalabopoulos and S. K. Hadjikakou, Mixed ligand–silver(I) complexes with anti-inflammatory agents which can bind to lipoxygenase and calf-thymus DNA, modulating their function and inducing apoptosis, *Metallomics*, 2012, **4**, 545–560.
15 C. N. Banti, A. D. Giannoulis, N. Kourkoumelis, A. Owczarzak, M. Kubicki and S. K. Hadjikakou, Novel metallo-therapeutics of the NSAID naproxen. Interaction with intracellular components that leads the cells to apoptosis, *Dalton Trans.*, 2014, **43**, 6848–6863.
16 C. N. Banti, L. Kyros, G. D. Geromichalos, N. Kourkoumelis, M. Kubicki and S. K. Hadjikakou, A novel silver iodide metalo-drug: Experimental and computational modelling assessment of its interaction with intracellular DNA, lipoxygenase and glutathione, *Eur. J. Med. Chem.*, 2014, **77**, 388–399.

17 V. Tsiatouras, C. N. Banti, A. M. Grześkiewicz, G. Rossos, N. Kourkoumelis, M. Kubicki and S. K. Hadjikakou, Structural, photolysis and biological studies of novel mixed metal Cu(I)-Sb(III) mixed ligand complexes, *J. Photochem. Photobiol., B*, 2016, **163**, 261–268.
18 C. N. Banti, V. Tsiatouras, K. Karanicolas, N. Panagiotou, A. J. Tasiopoulos, N. Kourkoumelis and S. K. Hadjikakou, Antiproliferative activity and apoptosis induction, of organo-antimony(III)–copper(I) conjugates, against human breast cancer cells, *Mol. Diversity*, 2020, **24**, 1095–1106.
19 D. Mahendiran, N. Pravin, N. S. P. Bhuvanesh, R. S. Kumar, V. Viswanathan, D. Velmurugan and A. K. Rahiman, Bis (thiosemicarbazone)copper(I) Complexes as Prospective Therapeutic Agents: Interaction with DNA/BSA Molecules, and In Vitro and In Vivo Anti-Proliferative Activities, *ChemistrySelect*, 2018, **3**, 7100–7111.
20 C. N. Banti, A. D. Giannoulis, N. Kourkoumelis, A. M. Owczarzak, M. Kubicki and S. K. Hadjikakou, Silver(I) metallo-drugs of anti-inflammatory agents salicylic acid and its derivative which modulate cells function, *J. Inorg. Biochem.*, 2015, **142**, 132–144.
21 S. K. Hadjikakou, P. Aslanidis, P. Karagiannidis, A. Aubry and S. Skoulika, Copper(I) complexes with tri-o-tolylphosphine and heterocyclic thione ligands. Crystal structures of [(pyrimidine-2-thione)(tri-o-tolylphosphine)copper(I) chloride] and [(pyridine-2-thione)(tri-o-tolylphosphine) copper(I) iodide], *Inorg. Chim. Acta*, 1992, **193**, 129–135.
22 V. I. Balas, C. N. Banti, N. Kourkoumelis, S. K. Hadjikakou, G. D. Geromichalos, D. Sahpazidou, L. Male, M. B. Hursthouse, B. Bednarz, M. Kubicki, K. Charalabopoulos and N. Hadjiliadis, Structural and In Vitro Biological Studies of Organotin(IV) Precursors; Selective Inhibitory Activity Against Human Breast Cancer Cells, Positive to Estrogen Receptors, *Aust. J. Chem.*, 2012, **65**, 1625–1637.
23 C. R. Groom, I. J. Bruno, M. P. Lightfoot and S. C. Ward, The Cambridge Structural Database, *Acta Crystallogr., Sect. B: Struct. Sci., Cryst. Eng. Mater.*, 2016, **72**, 171–179.
24 R. D. Hart, P. C. Healy, M. L. Peake and A. H. White, Anion Effects on the Structural Properties of Bis(triphenylphosphine)copper(I) Carboxylate Complexes [$(PPh_3)_2CuO_2CR$], *Aust. J. Chem.*, 1998, **51**, 67.
25 R.-N. Yang, T.-X. Li, Y.-A. Sun, X.-Y. Hu, D.-M. Jin and B.-S. Luo, Crystal and Molecular Structure of Copper(I) Complex [$Cu(PPh_3)_2(NO_3)$], *Jiegou Huaxue*, 2000, **19**, 126.
26 G. G. Messmer and G. J. Palenik, Crystal structure of bis(triphenylphosphine)copper(I) nitrate, *Inorg. Chem.*, 1969, **8**, 2750.
27 J. G. Małecki and A. Maroń, Luminescence properties of copper(I), zinc(II) and cadmium(II) coordination compounds with picoline ligands, *J. Lumin.*, 2017, **186**, 127.
28 C. Pettinari, G. G. Lobbia, G. Sclavi, D. Leonesi, M. Colapietro and G. Portalone, Synthesis and characterization of derivatives of copper(I) with n-donor ligands-I. Azole and bis(azolyl)alkane compounds. Crystal structure of nitrato bis(tri-p-tolylphosphine)copper(I), *Polyhedron*, 1995, **14**, 1709.
29 D. Saravanabharathi, Monika, P. Venugopalan and A. G. Samuelson, Solid state structural and solution studies on the formation of a flexible cavity for anions by copper(I) and 1,2-bis(diphenylphosphino)ethane, *Polyhedron*, 2002, **21**, 2433.
30 T. N. Hill and A. Roodt, (Nitrato-κO)tris[tris(4-fluorophenyl) phosphane-κP]copper(I), *Acta Crystallogr., Sect. E: Struct. Rep. Online*, 2012, **68**, m1396.
31 B. A. Babgi, S. Alsaedi, D. Domyati, A. Jedidi, B. Davaasuren, A.-H. M. Emwas and M. Jaremko, Electronic and steric factors affecting the ligands redistribution reaction of [Cu(2,2′-biquinoline)(PR3)2]+ systems in fluid solutions, *J. Mol. Struct.*, 2022, **1261**, 132933.
32 G. Steyl, Nitratotris(triphenyl-phosphine)copper(I) methanol solvate, *Acta Crystallogr., Sect. E: Struct. Rep. Online*, 2009, **65**, m272.
33 J. C. Dyason, L. M. Engelhardt, P. C. Healy, H. L. Klich and A. H. White, Lewis-Base Adducts of Group 11 Metal(I) Compounds. XXV. Synthesis and Structural Properties of Tris(Triphenylphosphine)Copper(I) Perchlorate and Nitrate, *Aust. J. Chem.*, 1986, **39**, 2003.
34 P. Karagiannidis, S. K. Hadjikakou, P. Aslanidis and A. Hountas, Synthesis and photochemical study of Cu(I) complexes with tri-p-tolylphosphine and heterocyclic thiones. The crystal structure of [$CuCl(pymtH)(p\text{-}CH_3C_6H_4)_3P]_2$, *Inorg. Chim. Acta*, 1990, **178**, 27–34.
35 S. K. Hadjikakou, P. Aslanidis, P. Karagiannidis, D. Mentzafos and A. Terzis, Synthesis and photolysis of mixed copper(I) complexes with thiones and tri-p-tolylphosphine or triphenylphosphine; X-ray crystal structure of bis [copper(I)(1,3-thiazolidine-2-thione) (tri-p-tolylphosphine) chloride], *Polyhedron*, 1991, **10**, 935–940.
36 S. K. Hadjikakou, P. Aslanidis, P. Karagiannidis, A. Hountas and A. Terzis, Synthesis and photolysis of a new series of Cu(I) complexes with tri-m-tolylphosphine and heterocyclic thiones. The crystal structure of bis[μ-iodo (pyridine-2-thione)(tri-m-tolylphosphine)copper(I)], *Inorg. Chim. Acta*, 1991, **184**, 161–166.
37 P. Karagiannidis, S. K. Hadjikakou and N. Papadopoulos, Electrochemical reduction of copper(I) mixed- ligand complexes with phosphines and heterocyclic thiones in acetonitrile solutions with glassy carbon electrodes, *Polyhedron*, 1992, **11**, 2947–2949.
38 P. M. Castro and P. W. Jagodzinski, FTIR and Raman spectra and structure of $Cu(NO_3)^+$ in aqueous solution and acetone, *Spectrochim. Acta, Part A*, 1991, **47**, 1707–1720.
39 N. Senkuttuvan, B. Komarasamy, R. Krishnamoorthy, S. Sarkar, S. Dhanasekaran and P. Anaikutti, The significance of chirality in contemporary drug discovery-a mini review, *RSC Adv.*, 2024, **14**, 33429–33448.
40 C. N. Banti, A. A. Piperoudi, C. P. Raptopoulou, V. Psycharis, C. M. Athanassopoulos and S. K. Hadjikakou, Mitochondriotropic agents conjugated with NSAIDs through metal ions against breast cancer cells, *J. Inorg. Biochem.*, 2024, **250**, 112420.

41 C. N. Banti, G. Vagenas, C. P. Raptopoulou, V. Psycharis, J. C. Plakatouras and S. K. Hadjikakou, Silver(I) Ions Bridging Oxadiazole-2-thione Derivatives with Mitochondriotropic Agents: A Promising Strategy for Potent Anticancer Chemotherapy, *Inorg. Chem.*, 2025, **64**, 13010–13029.
42 C. N. Banti, C. Papatriantafyllopoulou, C. Papachristodoulou, A. G. Hatzidimitriou and S. K. Hadjikakou, New Apoptosis Inducers Containing Anti-inflammatory Drugs and Pnictogen Derivatives: A New Strategy in the Development of Mitochondrial Targeting Chemotherapeutics, *J. Med. Chem.*, 2023, **66**, 4131–4149.
43 P. C. Dedon, Determination of Binding Mode: Intercalation, *Curr. Protoc. Nucleic Acid Chem.*, 2000, **8**, 8.1.1–8.1.13, John Wiley & Sons, Inc.
44 H. R. Drew, R. M. Wing, T. Takano, C. Broka, S. Tanaka, K. Itakura and R. E. Dickerson, Structure of a B-DNA dodecamer: conformation and dynamics, *Proc. Natl. Acad. Sci. U. S. A.*, 1981, **78**, 2179–2183.
45 C. Hu and S. Ma, Recent development of lipoxygenase inhibitors as anti-inflammatory agents, *MedChemComm*, 2018, **9**, 212–225.
46 G. M. Sheldrick, Crystal structure refinement with SHELXL, *Acta Crystallogr., Sect. C*, 2015, **71**, 3–8.
47 G. M. Sheldrick, A short history of SHELX, *Acta Crystallogr., Sect. A:Found. Crystallogr.*, 2008, **64**, 112–122.
48 O. V. Dolomanov, L. J. Bourhis, R. J. Gildea, J. A. K. Howard and H. Puschmann, OLEX2: a complete structure solution, refinement and analysis program, *J. Appl. Crystallogr.*, 2009, **42**, 339–341.
49 *CrystalClear*, Rigaku/MSC Inc, 2005 (The Woodlands Texas).
50 *DIAMOND - Crystal and Molecular Structure Visualization, Ver. 3.1, Crystal Impact*, Rathausgasse 30, 53111, Bonn, Germany.
51 O. Trott and A. J. Olson, AutoDock Vina: improving the speed and accuracy of docking with a new scoring function, efficient optimization, and multithreading, *J. Comput. Chem.*, 2010, **31**, 455–461.
52 G. M. Morris, R. Huey, W. Lindstrom, M. F. Sanner, R. K. Belew, D. S. Goodsell and A. J. Olson, AutoDock4 and AutoDockTools4: Automated docking with selective receptor flexibility, *J. Comput. Chem.*, 2009, **16**, 2785–2791.
53 (*a*) CCDC 2486986: Experimental Crystal Structure Determination, 2026, DOI: 10.5517/ccdc.csd.cc2pgxcg; (*b*) CCDC 2486987: Experimental Crystal Structure Determination, 2026, DOI: 10.5517/ccdc.csd.cc2pgxdh; (*c*) CCDC 2490244: Experimental Crystal Structure Determination, 2026, DOI: 10.5517/ccdc.csd.cc2pl9g2.